CHALMERS
UNIVERSITY OF TECHNOLOGY

UNIVERSITY OF GOTHENBURG

Design and Verification of Antennas for Tomographic Radar Systems in the Frequency Range 76–81 GHz

Master's thesis in Computer science and engineering

WAFA PATHAN RAHAMTULLA

Department of Computer Science and Engineering
CHALMERS UNIVERSITY OF TECHNOLOGY
UNIVERSITY OF GOTHENBURG
Gothenburg, Sweden 2019

Master's thesis 2019

Design and Verification of Antennas for Tomographic Radar Systems in the Frequency Range 76–81 GHz

WAFA PATHAN RAHAMTULLA

UNIVERSITY OF
GOTHENBURG

CHALMERS
UNIVERSITY OF TECHNOLOGY

Department of Computer Science and Engineering
Chalmers University of Technology
University of Gothenburg
Gothenburg, Sweden 2019

Advisor: Andreas Och, Danube Integrated Circuit Engineering GmbH Co. KG (DICE)
Supervisor: Prof. Jan Stake, Department of Microtechnology and Nanoscience
Examiner: Prof. Lena Peterson, Department of Computer Science and Engineering

Master's Thesis 2019
Department of Computer Science and Engineering
Chalmers University of Technology and University of Gothenburg
SE-412 96 Gothenburg
Telephone +46 31 772 1000

Gothenburg, Sweden 2019

Abstract

Microwave tomography is an imaging technique used to construct 3D images of the object under test using the principle of radar. Antennas in such systems are designed to obtain specific radiation characteristics to transmit and receive the signals. Antennas utilized for the purpose of radar generally radiate a fan shaped beam with high directivity in one plane and a wide beam in the orthogonal plane.

This thesis project focuses on the design, simulation, fabrication and characterization of antennas which will be integrated with a tomographic radar system being developed for noninvasive material characterization in the frequency range 76–81 GHz. The motive behind developing the antennas is that commercially available antennas do not satisfy the specifications.

The background theory of antennas is introduced and critical antenna parameters are identified. The design of the prototypes is based on specifications derived from the application. Two types of antennas – horn antenna and patch antenna array are designed as they each satisfy different system requirements more competently. The antennas are modelled according to the calculated approximate dimensions and simulated using finite element method simulations in ANSYS HFSS. In addition, optimization of different parameters is carried out to achieve the best antenna performance while fulfilling the system conditions.

The horn antenna was fabricated through 3D metal printing using two materials (steel and brass). The steel horn antenna has a half power beamwidth (HPBW) of 9.0° in the H-plane and 64.5° in the E-plane and a gain of 16 dB whereas the brass horn possesses a HPBW of 8.5° in the H-plane and 60.0° in the E-plane with a gain of 17.5 dB. Both the horn antennas cover the intended frequency range of 76–81 GHz. The second prototype produced is the patch antenna array with two variants differing in the size between the single patch elements. A HPBW of 17.0° in the E-plane and 60.0° in the H-plane with a gain of 14.4 dB was obtained for d=0.5 λ_g variant. For d=1.5 λ_g spacing, the HPBW was 6.5° in the E-plane and 63.0° in the H-plane with a gain of 12.9 dB. The bandwidth covered by each is 2.2 GHz and 3.89 GHz, respectively. Analysis of the results and comparison with the specifications show that the horn antenna and d=1.5 λ_g spacing patch antenna array satisfy the system specifications. The variant with d=0.5 λ_g partially satisfies the requirements and can be used in applications with size restrictions as it 50% less in length.

The tomographic radar system was simulated by considering one case of a transmitting and a receiving antenna with a glass slab. Increasing the distance of the glass from the transmitting antenna reduced the reflections. The glass produced the same effect as placing a lens in front of the antenna. The beam undergoes refraction at the air-glass boundary and bends towards the normal. The opposite effect takes place when the beam exits the glass.

The developed antennas can be utilized in different applications such as tomographic radar systems, medical and security applications which require the antennas to possess the specified radiation characteristics and operate over the frequency range 76–81 GHz.
Keywords: Antennas, RF, RADAR, FEM simulations, microwave engineering.

Acknowledgements

First and foremost, I would like to express my gratitude to my company supervisor, Andreas Och, for his continuous support and words of encouragement throughout my thesis. I would also like to acknowledge his recommendations for my writing. His guidance has helped me develop as a professional and as an individual. This thesis would not have been possible without him.
I want to thank my supervisor at Chalmers, Jan Stake, for his valuable comments and suggestions during my writing process . I also would like to extend my thanks to my examiner at Chalmers, Lena Peterson, who provided me with helpful feedback. Finally, I would like to thank my parents and sisters, who I am indebted to, for providing me an opportunity to pursue my interest and showing me unconditional support, and my friends who encouraged me whenever I needed it.

Wafa Pathan Rahamtulla, Gothenburg, December 2019

Contents

List of Figures **xi**

List of Tables **xiii**

1 Introduction **2**
1.1 Antennas in radar systems . . . 2
1.2 Tomography . . . 2
1.3 Motivation . . . 3
1.4 Thesis outline . . . 4

2 Theory **5**
2.1 Fundamental properties of antennas . . . 5
2.1.1 Radiation pattern . . . 5
2.1.2 Field regions . . . 6
2.1.3 Efficiency . . . 7
2.1.4 Directivity and gain . . . 8
2.1.5 Beamwidth . . . 8
2.1.6 Input impedance . . . 8
2.1.7 Bandwidth . . . 9
2.1.8 Polarization . . . 9
2.2 S-parameters . . . 10
2.3 Overview of antenna types . . . 12
2.4 Horn antennas . . . 13
2.4.1 Wave propagation . . . 13
2.4.2 H-Plane sectoral horn antenna . . . 14
2.5 Patch antennas . . . 15
2.5.1 Transmission line model . . . 16
2.5.2 Patch antenna feeding techniques . . . 16
2.5.3 Overview of rectangular patch antenna parameters . . . 18
2.6 Antenna arrays . . . 19
2.6.1 Linear arrays . . . 19
2.6.2 Antenna array feeding techniques . . . 20

3 Methods **22**
3.1 System specifications . . . 22
3.1.1 Frequency and bandwidth . . . 22
3.1.2 Half power beam width . . . 22

3.1.3 Reflection coefficient (S_{11}) . . . 23
3.1.4 Gain . . . 23
3.1.5 Impedance . . . 23
3.1.6 Polarization . . . 24
3.1.7 Maximum dimensions of prototypes . . . 24
3.2 Design of H-plane sectoral horn antenna . . . 24
3.3 Design of single patch element . . . 25
3.4 Design of patch antenna array . . . 26
3.5 Simulation workflow . . . 28
3.5.1 Modelling of structures . . . 28
3.5.2 Simulation settings . . . 30
3.5.3 Simulation of horn antenna prototype . . . 30
3.5.4 Simulation of patch antenna array prototype . . . 33
3.6 Fabrication of antenna prototypes . . . 35
3.6.1 3D printed horn antennas . . . 35
3.6.2 Fabricated patch antennas on PCB . . . 38
3.7 Measurement setup . . . 41
3.7.1 Measurement procedure . . . 42
3.8 Deembedding of patch antennas . . . 45
3.9 Measurement repeatibility . . . 47

4 Results **48**
4.1 Horn antenna . . . 48
4.2 Patch antenna array . . . 50
4.3 System setup . . . 53
4.3.1 Return loss measurements . . . 54
4.3.2 Refraction . . . 56

5 Conclusion **59**
5.1 Discussion . . . 59
5.2 Future work . . . 60
5.2.1 Horn antenna . . . 60
5.2.2 Patch antenna . . . 60

Bibliography **61**

List of Figures

1.1 Tomographic radar system 4

2.1 3D radiation pattern 5
2.2 2D radiation pattern 6
2.3 Field regions around an antenna 7
2.4 Relation between impedance Z_{A}, resistance R_{A} and reactance X_{A} . . 8
2.5 Linear,circular and elliptical polarization 10
2.6 S-parameters in a 2-port network 11
2.7 S-parameters in antenna network 12
2.8 Different types of horn antennas 13
2.9 Geometry of the H-plane sectoral horn 14
2.10 Phase error in H-plane sectoral horn 15
2.11 Tranmission line model 16
2.12 Fringing effect 17
2.13 Different types of antenna feeding techniques 18
2.14 Linear antenna array 20
2.15 Parallel and series feeding techniques 21

3.1 Derivation of HPBW specifications 23
3.2 HPBW as a function of flare angle α for different horn lengths R_1 [1]. 25
3.3 Beamwidth as a function of array factor for different number of elements 27
3.4 Design parameters of 10 element patch antenna array 28
3.5 Airbox in HFSS 29
3.6 Symmetry planes in HFSS 29
3.7 Model of horn antenna with standard WR-12 waveguide flange. . . . 31
3.8 Strength of fields in the H-plane radiated backwards 31
3.9 Oscillations observed in the gain due to constructive and destructive interference 32
3.10 Model of patch antenna array with element spacing 0.5 λ_{g}. 33
3.11 Effect of variation in patch length on resonant frequency 34
3.12 Model of patch antenna array with element spacing d=1.5 λ_{g} 35
3.13 Manufactured horn antenna prototypes 36
3.14 Effect of production tolerances on horn prototypes 37
3.15 Manufactured PCB with three variants 38
3.16 Close up of the manufactured PCB 38
3.17 Effect of expansion and shrinkage of patch array dimensions 39
3.18 Patch antenna array with 0.5 λ_{g} spacing under a microscope 39

3.19 Shrinkage of patch antenna array dimensions 40
3.20 Scratches of gold surface finish and holes seen in array 40
3.21 Measurement setup 41
3.22 Description of gain comparison method 42
3.23 Reference measurement setup 44
3.24 Setup with DUT and reference antenna for E-plane measurements. . . 44
3.25 Deembedding of patch antennas 45
3.26 Signal flow graph of the calibration structure 46
3.27 Signal flow graph of model used for deembedding 46
3.28 Comparison of four iterations of the same S_{11} measurement under the same test conditions is plotted. The standard deviation has a maximum value of 0.038. 47

4.1 S_{11} results of horn antenna prototypes 48
4.2 S_{21} results of horn antenna prototypes 49
4.3 2D and 3D simulated radiation pattern of horn antenna 49
4.4 S_{11} results of patch antenna array 50
4.5 S_{21} results of patch antenna array 51
4.6 Reduction in electric field strength between patch elements 52
4.7 2D and 3D simulated radiation pattern of patch antenna with d=0.5 λ_g 52
4.8 2D and 3D simulated radiation pattern of patch antenna with d=1.5 λ_g 52
4.9 Tomographic system modelled in HFSS 53
4.10 Simplified setup of the tomographic system 54
4.11 Effect of different distances of glass from antenna on S_{11} 55
4.12 Snell's law 56
4.13 Lens effect due to glass on horn antenna radiation pattern 57
4.14 Effect of refraction on H-plane and E-plane radiation pattern of horn antenna 58
4.15 Effect of glass on patch antenna array radiation pattern 58

List of Tables

2.1 Comparison of different antenna types used at microwave frequencies 12
2.2 Comparison of different feeding techniques for patch antennas 17

3.1 HPBW for different horn lengths R_1 with flare angle $\alpha = 20°$. 24
3.2 Calculated horn antenna dimensions and design parameters 26
3.3 Calculated parameters of single patch antenna 26
3.4 Dolph-Chebyshev coefficients for a 10 element patch antenna array . . 27
3.5 Comparison of calculated and optimized values for horn antenna. . . 32
3.6 Degree of influence of various parameters on the design 33
3.7 Comparison of calculated and optimized values for patch antenna array 34
3.8 Scaling factors of the manufactured horn prototypes 36
3.9 Comparison of designed and measured dimensions of horn prototype . 37
3.10 Settings of VNA 41

4.1 Comparison of simulated and measured results 53

List of Abbreviations

DUT	device-under-test
HFSS	high frequency structure simulator
HPBW	half power beamwidth
MT	microwave tomography
NDE	non destructive evaluation
PCB	printed circuit board
RX	receiving
TRL	through-line-reflect
TX	transmitting
VNA	vector network analyzer

1
Introduction

1.1 Antennas in radar systems

Radar systems use electromagnetic waves for detection of range, velocity or position of objects. They usually consist of transmitting (TX) antennas and receiving (RX) antennas. The function of an antenna is to convert the electrical energy in the transmitted signal to electromagnetic energy radiated into the medium, usually free space. The TX antennas radiate concentrated energy in a desired direction. The RX antennas intercept parts of the reflected signal which are processed to obtain information about the presence of an object, its position and relative velocity. The TX and RX antennas are often of the same type [2].

Radar antennas for automotive applications are characterized by highly directional beams having narrow beamwidths in one plane to focus energy on the objects and a wide beam in the other plane to scan a larger area. This narrow beam results in accurate measurements and better resolution to distinguish different closely spaced targets. For a given antenna aperture, the beamwidth is inversely proportional to the frequency. Hence, microwave frequencies are beneficial for radar applications [2].

The use of frequency bands for radar is well regulated. The bands allocated for automotive radar are 24–24.25 GHz and 76–81 GHz [3]. For 24 GHz, the maximum bandwidth is limited to 250 MHz by law in most parts of the world [4]. The shift from the 24 GHz to the 76–81 GHz range is because the latter has smaller wavelength which reduces the antenna sizes and makes the antennas more compact [5]. The decrease in size allows the antennas and sensors to be mounted with ease. The 76–81 GHz frequency range also has larger bandwidth and features such as high-range resolution and better accuracy which are important for automotive radar and industrial level sensing [6]. Advantages of using this frequency range include ability to penetrate materials, high directionality, and large bandwidths [7]. Therefore, the development of different types of antennas in the 76–81 GHz frequency range for various applications such as radar has been of great interest in recent years [4, 7].

1.2 Tomography

Tomography is an imaging technique that reconstructs 3D images of objects from 2D slices. This approach is utilized to locate the position of the object under test and identify their size. Different materials inside the observation area are distinguishable

due to the difference in their electromagnetic properties such as dispersion, dielectric permittivity and attenuation [8, 9].

Microwave tomography (MT), which employs the principle of radar, is a method of non-destructive evaluation (NDE) widely used to analyze the characteristics of a target material inside the imaging region [10, 11]. MT systems are usually complex to design and the various challenges include the configuration of the system, the procedure of obtaining data, evaluating the data and processing it to reconstruct 3D images of the object [12].

The two main steps in applying the technique of MT are data collection and data processing. Data is collected when the target object is illuminated by multiple transmit antennas and the resulting scattered microwave fields are measured using receive antennas. The resulting data is processed to create a profile of the object in multi-dimensional views. A large number of antennas can collect an extensive data set but this is usually limited due to size restrictions of the system [13]. The antennas are one of the main components of an MT system as they transmit and receive the signals which are processed using sensors to acquire the data for image reconstruction. Therefore, suitable antenna types should be chosen according to the intended application and configuration of the system.

MT is applied in various fields such as industrial level material characterization for the assessment of flaws and blockages in metal or concrete [14, 15], biomedical imaging [16–18] and security applications.

1.3 Motivation

A novel tomographic radar system is being developed for industrial applications such as noninvasive material characterization of gas mixtures or granular plastics which are transported in a metal pipe. The object under test is surrounded by several radar modules constituting the system as seen in Fig. 1.1. The multi-dimensional distribution of material properties is reconstructed by combining multiple single-dimensional measurements in post-processing. The measurements are carried out using the time-of-flight principle which determines the time taken by the transmitted signal to reach the receiver. The scattered waves can be used to derive information about the changes in the electromagnetic fields which gives an estimate about the shape and position of the object. This measured time will vary for different materials depending on their permittivity which can then be used to characterize them.

The antenna prototypes developed in this thesis are intended to be used in such a tomographic radar system. The antenna prototypes are designed to have a wide beam in one plane and a narrow beam in the orthogonal plane similar to antennas used in other radar systems. This configuration, when applied to the tomographic radar system currently being developed, helps to focus the energy of the transmitted signal in the desired region where the object under test is located while reducing unwanted reflections from the metallic sides of the pipe. The reason for development of the antenna prototypes is that they are not commercially available for the intended frequency range with the desired performance characteristics.

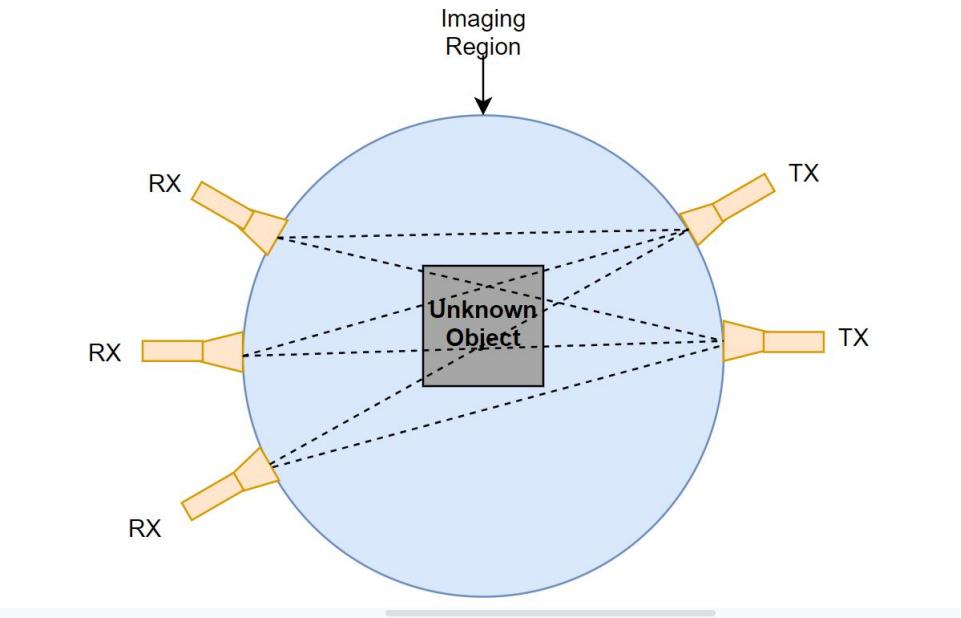

Figure 1.1: A tomographic system arrangement with two transmit antennas and three receive antennas is shown. The target is located inside the imaging area and electromagnetic waves radiated from multiple antennas are incident on the object at different angles and the scattered waves are measured by the receiving antennas.

1.4 Thesis outline

The first chapter provides a brief introduction to radar systems and MT in relation to antennas. Additionally, the purpose of developing antenna prototypes for a tomographic radar system is explained.

The second chapter focuses on the theoretical background that is important to understand this project. It provides an overview of the essential antenna parameters considered while designing an antenna. Different antenna types at microwave frequencies are compared and the models and design parameters unique to the chosen antenna types are explained in further detail. Antenna arrays are also discussed briefly.

The third chapter delineates the detailed designing of the horn antenna and patch array antenna according to the system specifications. It outlines the considerations taken into account while running simulations. The fabrication process used for both the antenna types is explained. The measurement setup is described along with the process of evaluating the raw data.

The fourth chapter analyses the results obtained in simulation and measurements and provides a comparison between them. Stand-alone antenna results are presented along with results of the antennas integrated in a mock setup of the tomographic system.

The fifth chapter draws conclusions from the results and includes a brief summary of the outcomes of this project. Areas of future work are also discussed.

2

Theory

2.1 Fundamental properties of antennas

An overview of important parameters describing the performance of an antenna is given in this chapter. Few of these parameters may be of higher significance than others depending on the intended application and the design process should focus on these key parameters.

2.1.1 Radiation pattern

A radiation pattern is a graphical representation of the distribution of the radiated energy as a function of space coordinates. It is a 3D pattern as shown in Fig. 2.1 but often a 2D slice along the horizontal or vertical planes is displayed.

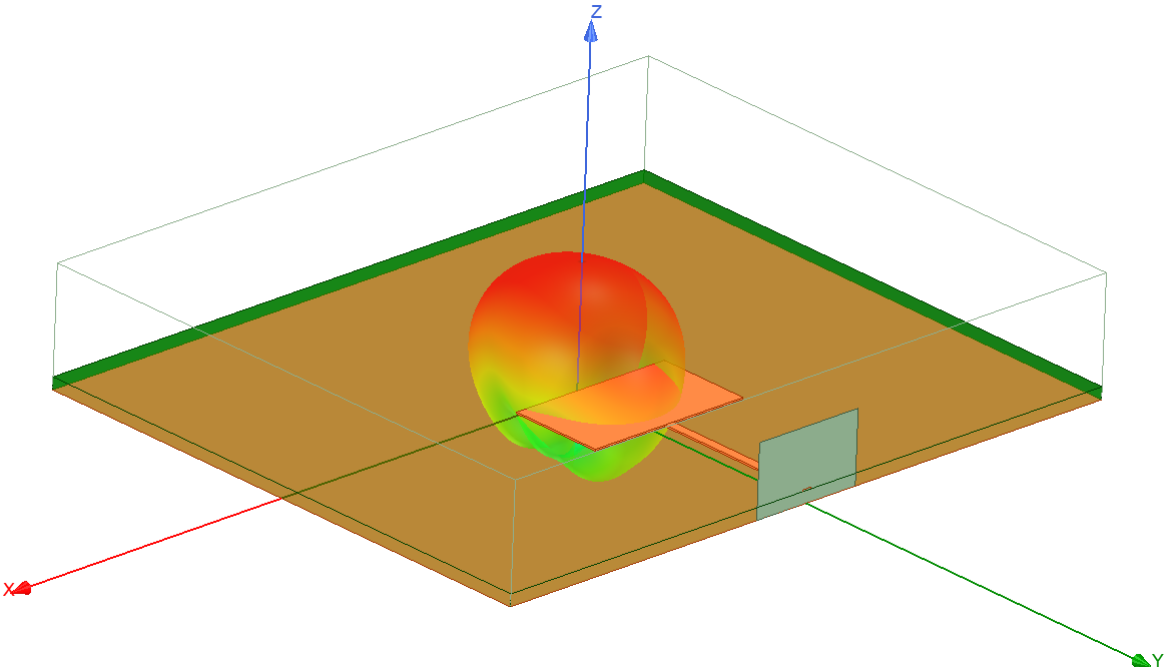

Figure 2.1: Exemplary 3D polar plot of radiation pattern representing the spatial distribution of radiated energy.

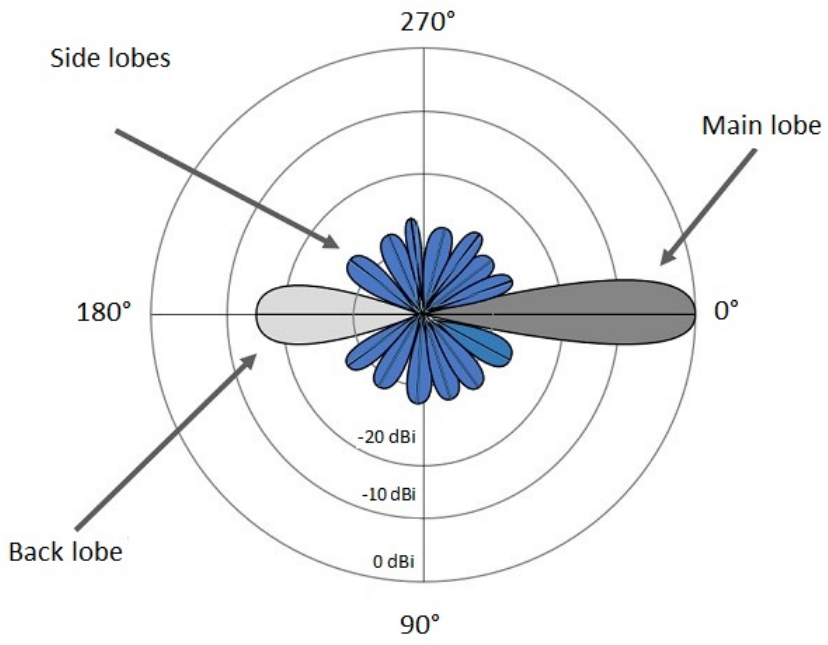

Figure 2.2: Exemplary radiation pattern in 2D showing main lobe and back lobe along with multiple side lobes [19].

Fig. 2.2 shows an exemplary radiation pattern which consists of a main lobe, multiple side lobes and a back lobe. The main lobe signifies the direction of maximum radiation of the antenna. The lobes in a direction other than the main lobe are called side lobes and are generally undesirable since they radiate energy in unwanted directions. Side lobe level (SLL) is the ratio of the maximum amplitude of the main beam a_{M} to the maximum amplitude of the highest side lobe a_{SL}.

$$SLL = \frac{max(a_{\mathrm{M}})}{max(a_{\mathrm{SL}})} \tag{2.1}$$

The back lobe, whose amplitude varies considerably according to the antenna type, appears in the direction opposite to the main lobe.

2.1.2 Field regions

The radiation space around an antenna is divided broadly into three regions – reactive near-field region, radiative near-field region (Fresnel) and far-field region depicted in Fig. 2.3.
The near-field region is the region closest to the antenna. The electric and magnetic fields in the near-field region are not orthogonal and difficult to predict. The field distribution depends on the distance from the antenna. Most analytical models do not apply in near-field conditions. In the reactive near-field region, not all the energy is radiated and some of it might be stored in the antenna [20]. The boundary of the reactive near-field region R_1 is expressed as:

$$R_1 < 0.62 \sqrt{\frac{D^3}{\lambda}} \tag{2.2}$$

where D is the largest dimension of the antenna and λ is the wavelength in free space.
The radiative near-field region describes a transition zone between the near-field and far-field region where radiation behaviour dominates. There is no abrupt change in the fields at the boundaries defined but rather a smooth transition. The region occupied by the radiative near-field region R_2 lies between:

$$0.62\sqrt{\frac{D^3}{\lambda}} < R_2 < \frac{2 \cdot D^2}{\lambda} \tag{2.3}$$

The far-field region extends from the boundary of the near-field to infinity. The distance of the wave from the antenna no longer determines the field distribution. Analytical solutions and approximations can be applied to the antenna and its electric and magnetic fields are orthogonal [20]. The boundary of the far-field region R_3 is expressed in the following way:

$$R_3 > \frac{2 \cdot D^2}{\lambda} \tag{2.4}$$

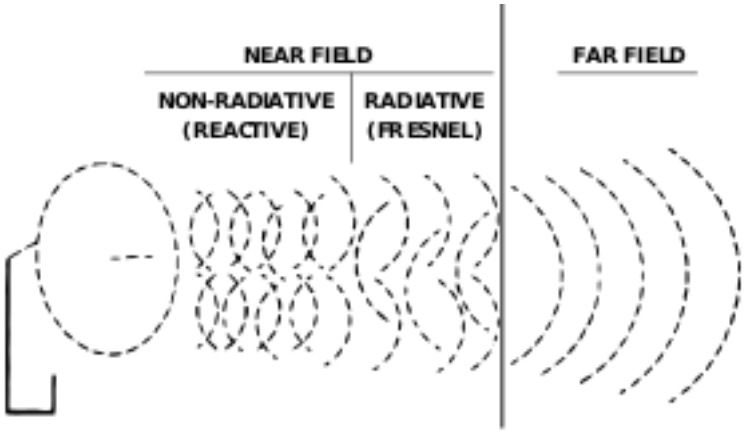

Figure 2.3: Behaviour of the fields of the propagating wave shown in different regions surrounding the antenna, namely reactive near-field, radiative near-field and far-field [20].

2.1.3 Efficiency

The antenna efficiency, also called radiation efficiency η, is the ratio of the radiated power P_{radiated} to the input power P_{input} of the antenna [21]:

$$\eta > \frac{P_{\text{radiated}}}{P_{\text{input}}} \tag{2.5}$$

It describes the ability of an antenna to convert electrical power into radiated power. An antenna has high efficiency if most of the input power is radiated away. On the contrary, the efficiency is low if the input power is absorbed, due to losses in the antenna such as conduction and dielectric losses, or reflected due to impedance mismatch.

2.1.4 Directivity and gain

Directivity D refers to the ability of the antenna to concentrate the signal energy in a particular direction and determines the shape of the radiated beam. Antenna gain G additionally takes radiation efficiency η into account expressed as [22]:

$$G = \eta D \tag{2.6}$$

Gain determines the amount of power contained in the beam. Calculation of gain is done by comparing the transmitted or received power of the antenna to the transmitted or received power of an isotropic antenna under the same conditions. An isotropic antenna radiates the signal energy equally in all directions. Gain is usually expressed in dBi.

$$G_{\mathrm{dBi}} = 10 \cdot \log_{10} G \tag{2.7}$$

2.1.5 Beamwidth

Beamwidth is defined as the angular separation between two identical points on either side of the maximum main beam amplitude. The half power beamwidth (HPBW) specifically refers to the angle between the two points where the magnitude of the main beam decreases by 3 dB or 50% of the peak. The horizantal beamwidth θ and vertical beamwidth β are related to the gain of the antenna G according to the equation [1]:

$$G \approx \frac{30000}{\theta \cdot \beta} \tag{2.8}$$

2.1.6 Input impedance

Input impedance of an antenna is defined as the ratio of voltage to current at the input terminals. The impedance is expressed as a complex number which includes the effects of resistance represented by the real part R_{A} and the effects of reactance represented by the imaginary part X_{A}.

$$Z_{\mathrm{A}} = R_{\mathrm{A}} + jX_{\mathrm{A}} \tag{2.9}$$

R_{A} remains constant as it does not depend on frequency whereas X_{A} varies with frequency as it is a measure of inductive reactance and capacitive reactance. The antenna will resonate at the frequency where the imaginary part of the impedance is zero.

$$X_{\mathrm{A}} = X_{\mathrm{L}} - X_{\mathrm{C}} \tag{2.10}$$

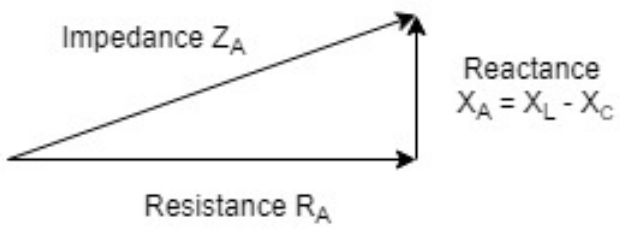

Figure 2.4: Relation between impedance Z_{A}, resistance R_{A} and reactance X_{A} which includes the effect of inductive X_{L} and capacitive X_{C} reactance.

The impedance of a wave Z at any point is defined as the ratio of the transverse components of electric field E to the magnetic field H_0 given by:

$$Z = \frac{E_0}{H_0}. \tag{2.11}$$

The wave impedance is a property of the wave, characterized by the medium through which it travels, expressed as:

$$Z = \sqrt{\frac{j\omega\mu}{\sigma + j\omega\varepsilon}}, \tag{2.12}$$

where ω is the angular frequency of the wave, μ is magnetic permeability, σ is the conductivity of the medium and ε is electric permittivity.

If the medium is considered to be air or vacuum, then the wave impedance is:

$$Z \approx \sqrt{\frac{\mu}{\varepsilon}} \approx 377\,\Omega. \tag{2.13}$$

Impedance matching is a method used to match the output impedance of the driving source to the antenna's input impedance usually taken as $50\,\Omega$ which is an industry standard. Better impedance matching maximizes power transfer and minimizes reflection losses. If the impedance of the antenna input is Z_{A} and impedance of the port output is Z_{L}, then the matched condition under which maximum power transfer occurs is:

$$Z_A = Z_{\mathrm{L}}^* \tag{2.14}$$

If the above condition is not satisfied, a matching circuit or structure is required which transforms the impedance for instance R-L-C circuits, transmission lines or transformers [23].

2.1.7 Bandwidth

The bandwidth of the antenna refers to the range of frequencies over which the antenna performance is acceptable with respect to a specified standard. The standard is often chosen as the level of input reflected power below -10 dB or -15 dB. As bandwidth is relative to frequency, it is generally calculated as percentage:

$$BW = \frac{f_H - f_L}{f_C} \times 100\%, \tag{2.15}$$

where f_{H} is the upper cutoff frequency, f_{L} is the lower cutoff frequency and f_{C} is the center frequency of the antenna [1].

2.1.8 Polarization

The polarization of an antenna refers to the orientation of the radiated fields with respect to time when evaluated in the far field. The polarization of the transmitting and receiving antenna need to be same for effective communication. Polarization of a wave describes the direction and magnitude of the electric field vector as the wave

propagates. In elliptical polarization, the electric field vector has a time varying magnitude and rotates in an elliptical path [24]. Elliptical polarization as well as its two specialized cases, linear and circular polarization, are depicted in Fig. 2.5.

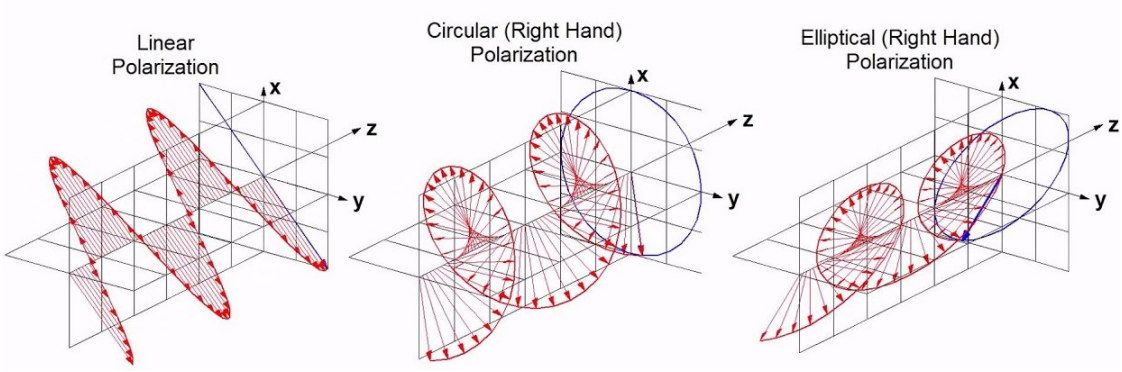

Figure 2.5: Different types of polarization classified as linear, circular and elliptical based on the paths traced by the tip of the electric field vector components [24].

In linear polarization, the electric field vector propagates in only a single plane (horizontal or vertical) with constant magnitude. In circular polarization, the electric field vector remains constant in length and traces a circular path with time. It can be further classified as left handed circular polarization (LHCP) or right handed circular polarization (RHCP) depending on the direction of rotation of the wave [21].

If the transmitter and receiver antennas both have opposite linear polarization (horizontal and vertical) or opposite circular polarization (RHCP and LHCP), total attenuation due to mismatch occurs and no power is received [22]. This is used as a method to decouple antennas spaced in the vicinity of each other.

2.2 S-parameters

The scattering parameters give information about the electrical behavior of a device-under-test. For a multi-port network, S_{AB} denotes the power transferred to port A from port B. For a two-port network, the scattering parameters are S_{11} and S_{22} also called reflection coefficients, together with S_{12} and S_{21} which are the transmission coefficients [25]. These are shown in Fig. 2.6.

The S-parameters can be written in a matrix as:

$$S = \begin{bmatrix} S_{11} & S_{12} \\ S_{21} & S_{22} \end{bmatrix} \tag{2.16}$$

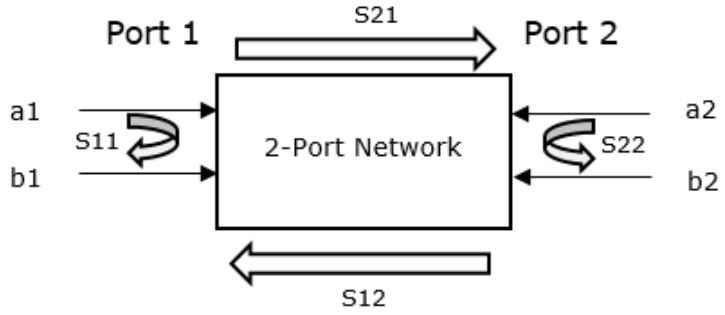

Figure 2.6: S-parameters in a 2-port network

An important condition that can be deduced from the matrix for a lossless network is the relation between the reflection and transmission coefficients given by [25]:

$$|S_{11}|^2 + |S_{21}|^2 = 1 \tag{2.17}$$

$$|S_{22}|^2 + |S_{12}|^2 = 1 \tag{2.18}$$

The incident and reflected wave variables defined in terms of current I, voltage V and impedance Z_0 are given by a_1 and b_1 along with a_2 and b_2 at port 1 and port 2, respectively [25].

$$a_1 = \frac{V_1 + Z_0 I_1}{2\sqrt{Z_0}} \tag{2.19}$$

$$a_2 = \frac{V_2 - Z_0 I_2}{2\sqrt{Z_0}} \tag{2.20}$$

$$b_1 = \frac{V_1 - Z_0 I_1}{2\sqrt{Z_0}} \tag{2.21}$$

$$b_2 = \frac{V_2 + Z_0 I_2}{2\sqrt{Z_0}} \tag{2.22}$$

The wave variables are related to the S-parameters by the following equations [25]:

$$b_1 = S_{11}a_1 + S_{12}a_2 \tag{2.23}$$

$$b_2 = S_{21}a_1 + S_{22}a_2 \tag{2.24}$$

The two-port network model can also be applied to antennas as shown in Fig. 2.7. The transmitting antenna, also called test antenna, is defined as the first port and the receiving antenna, also called reference antenna, is defined as the second port in the model. Eq. (2.17) and (2.18) do not hold true anymore since losses such as free space loss and mismatch loss have to be accounted for [25].

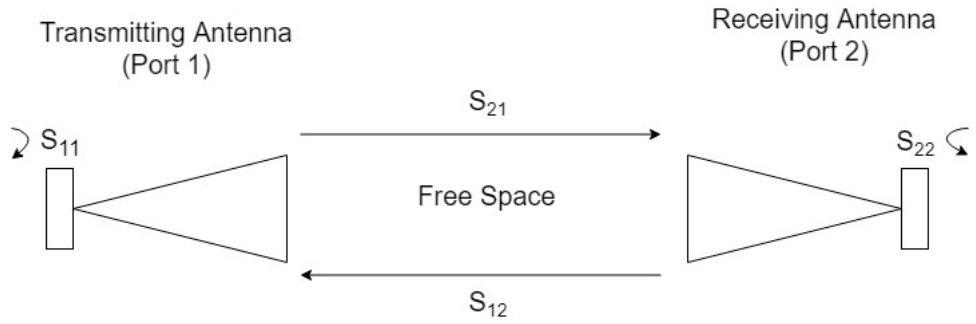

Figure 2.7: Antenna network adapted to the S-parameter model shows the coefficients S_{11}, S_{22}, S_{12} and S_{21} along with transmitting antenna as port 1 and receiving antenna as port 2.

The most important S-parameter for antennas is S_{11} as it ascertains proper functioning of the antenna in the specified frequency range. S_{11} also requires only one antenna to be measured. S_{11} signifies the amount of power reflected back to the signal source. A typical cause of this loss is reflected waves due to impedance mismatch between the source and load. If S_{11} is 0 dB, it implies that all of the power is reflected at the antenna. A well designed impedance match gives less reflections [26].

2.3 Overview of antenna types

Different antenna types are suitable for operation at particular frequencies. The most common types used at microwave frequencies are compared in Table 2.1.

Type of Antenna	Cost of Fabrication	Ease of Integration	Design Complexity	Bandwidth	Gain	Efficiency
Patch Array	Medium [27]	High	Complex	Low [28–30]	Medium [1]	Low [1]
Horn	Low to high [31]	Medium	Simple	High [32, 33]	High [32, 33]	High [32, 33]
PCB Slot	Low [34]	High	Simple	High [35]	Low [35]	Low [36]
Parabolic	High	Low	Complex	High [37]	High [37]	High [37]

Table 2.1: Comparison of different antenna types used at microwave frequencies with respect to metrics such as cost of fabrication, ease of integration, design complexity, bandwidth, gain and efficiency.

A patch antenna array and printed circuit board (PCB) slot antenna can be easily integrated onto planar and non-planar surfaces, whereas the horn and parabolic antenna are difficult to integrate into compact systems due to their large size. The patch antenna array has the lowest bandwidth as compared to the other types. The horn and parabolic antenna have higher gain and efficiency in contrast to the PCB slot and patch array antenna.

As seen from the comparison, patch array antenna and horn antenna would be the most suitable designs for the intended application discussed in more detail in section 1.3. A single antenna type is not ideal with respect to all parameters. Hence, the most suitable one can be chosen depending on the system constraints posed.

2.4 Horn antennas

A horn antenna is a waveguide section which is flared at one end to create an opening in one or both directions. In general, the waveguide cross-section has different dimensions in both planes. The plane containing the electric field is called the E-plane and the plane containing the magnetic field is called the H-plane. If the horn flares along both E-plane and H-plane dimensions, it is called a pyramidal horn. Flaring in either only the electric or magnetic planes results in an E-plane or H-plane sectoral horn, respectively, as shown in Fig. 2.8.

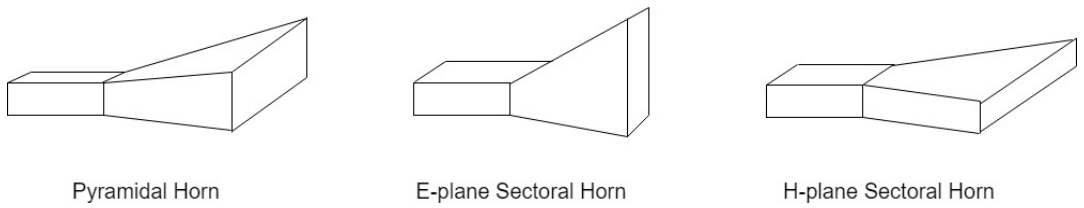

Figure 2.8: Direction of flaring resulting in different types of horns such as pyramidal horn, E-plane sectoral horn and H-plane sectoral horn.

The shape of the horn transitions the transmitted wave from the waveguide medium to free space smoothly. This transition over the length of the flare minimizes reflections and increases bandwidth. Horns operate over a wide range of frequencies since they are non-resonant antennas [1].

2.4.1 Wave propagation

Waveguides support the propagation of multiple modes of the electromagnetic wave. Modes are solutions derived from Maxwell's equations. Wave propagation in a waveguide occurs only when a particular cutoff frequency is met. Each mode has a lower cutoff frequency determined by the largest dimension of the waveguide section and is equal to $\lambda/2$. They exhibit different properties and it is essential to excite the desired mode and suppress the others. The dominant mode propagates when the lowest cutoff frequency is met.

The different types of waveguide modes are transverse electric (TE) where no electric field exists in the direction of propagation and transverse magnetic (TM) where no magnetic field exists in the direction of propagation. These modes are termed as $\mathrm{TE_{mn}}$ and $\mathrm{TM_{mn}}$ where m and n are integers representing the mode number. Generally, the dominant mode $\mathrm{TE_{10}}$ is preferred as the attenuation losses are minimum and its field distribution is predictable by wave theory.

The cutoff frequency of a particular mode for given geometric dimensions of the waveguide a and b is expressed using the following equation:

$$f_c = \frac{c}{2}\sqrt{\left(\frac{m}{a}\right)^2 + \left(\frac{n}{b}\right)^2} \tag{2.25}$$

For the dominant mode represented by m=1 and n=0, (2.25) reduces to:

$$f_c = \frac{c}{2a}. \tag{2.26}$$

2.4.2 H-Plane sectoral horn antenna

The characteristics of a horn antenna are attributed to the length, angle and direction of flare. A sectoral horn is able to produce a fan-shaped beam which is the desired beam shape as explained in section 3.1. H-plane sectoral horn has a larger beamwidth in the non-flared plane than the E-plane sectoral horn due to larger waveguide dimensions of the horn in that plane.

A sectoral horn antenna's geometry can be described by flare angle α, flare length R_{H}, axial length l_{H}, horn length R_1, width of the waveguide a, height of the waveguide b and width of the aperture A as shown in Fig. 2.9.

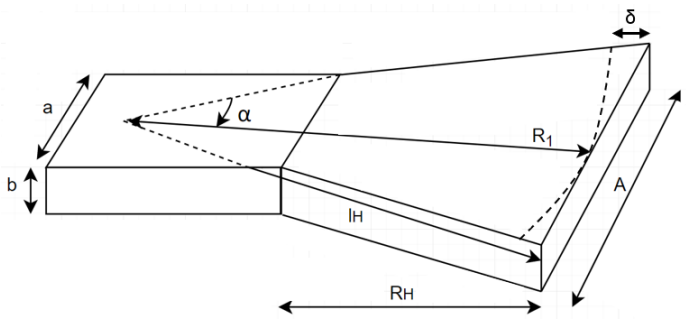

Figure 2.9: Geometry of the H-plane sectoral horn described using different design parameters such as flare angle α, flare length R_{H}, axial length l_{H} and horn length R_1.

The relation between the parameters is found by geometrical analysis [1]:

$$A = 2 \cdot R_1 \cdot \tan\alpha, \tag{2.27}$$

$$l_{\mathrm{H}}^2 = R_1^2 + \left(\frac{A^2}{2}\right), \tag{2.28}$$

$$R_{\mathrm{H}} = (A - a)\sqrt{\left(\frac{l_{\mathrm{H}}}{A}\right)^2 - \frac{1}{4}}. \tag{2.29}$$

Assuming spherical waves are radiated, the waves travelling a distance of axial length l_{H} and horn length R_{H} do not cover the same path length causing a phase error of δ as seen in Fig. 2.10. This phase error is negligible for a small flare angle α. However, for a given R_1, larger α results in a higher phase error δ. Hence, an optimum α exists for a particular R_1 beyond which the phase error cannot be ignored [38].

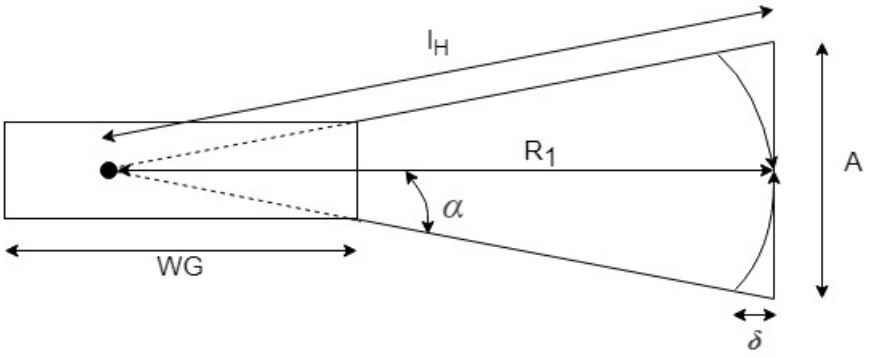

Figure 2.10: Phase error caused by spherical waves travelling different distances between the apex of the horn antenna to the aperture.

The aperture size is the product of the width A and height b of the opening of the horn and increases with α and R_H. Larger aperture size results in higher gain [22]. Though horns with high gain may be desired in some applications, large size makes the horns difficult to integrate. A trade-off between antenna size or gain should be reached [1].

2.5 Patch antennas

A patch antenna consists of a metallic patch on a dielectric substrate which is placed above a conducting ground plane. The patch is usually fabricated on top of the dielectric substrate by etching, a standard PCB manufacturing process. Different configurations of the patch include rectangular, square, circular or triangular. Rectangular and circular patch antennas are the most commonly used geometries. Rectangular shaped patch is selected for the design due to better gain and S_{11} than circular patch [39]. A patch is a resonant antenna which means the performance of its parameters changes significantly with frequency.

Various parameters are considered for the design of the patch antenna. An important decision is the selection of the dielectric material of the substrate as several metrics such as antenna dimensions, gain and beamwidth depend on it. Typical values of the dielectric constant ε_r lie between 2.2 and 12 [1]. A low dielectric constant along with a thick substrate facilitates a large bandwidth and high radiation efficiency as the fields are loosely bound in contrast to a thin substrate with high dielectric constant, which covers a smaller bandwidth and possesses lower radiation efficiency due to tightly bound fields. However, thick substrates increase the antenna size, weight and dielectric loss. A trade-off between radiation efficiency and bandwidth is achieved with thin substrates having low dielectric constant [40].

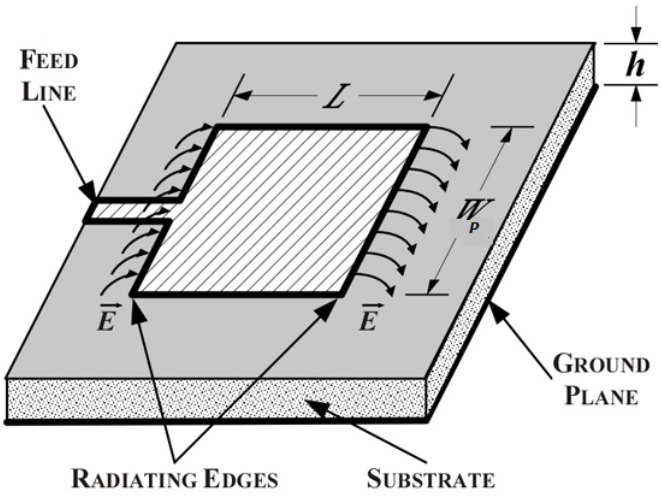

Figure 2.11: Analyzing rectangular patch antenna placed above a ground plane using transmission line model assuming two radiating slots with width W_P, height h and distance L between them [41].

2.5.1 Transmission line model

Multiple models exist for analysis of patch antennas which include transmission line model, cavity model and full wave model. The transmission line model is used in the following analysis as it is the least complex and gives accurate results for thin substrates. This model considers the antenna to be made up of two parallel radiating slots each of width W_p and height h with a transmission line of length L in between. The patch is surrounded by two different dielectric materials, usually air on top and the dielectric substrate below. From Fig. 2.12, it is clear that most of the electric field lines reside within the substrate between the metallized surfaces of the patch and ground plane but a few of the electric field lines also travel partly through air. This is called the fringing effect. The edges of the patch undergo fringing as the electric field does not end at the edges. The fringing effect reduces for a large L and smaller h as this configuration increases the number of field lines concentrated in the substrate. The parameter 'effective dielectric constant' $\varepsilon_{\mathrm{r,eff}}$ accounts for fringing and models a virtual homogeneous material which has similar electrical characteristics to the two dielectrics surrounding the patch:

$$\varepsilon_{\mathrm{r,eff}} = \frac{\varepsilon_\mathrm{r}+1}{2} + \frac{\varepsilon_\mathrm{r}-1}{2}\left[1+12\frac{h}{W_\mathrm{p}}\right]^{-0.5}. \tag{2.30}$$

2.5.2 Patch antenna feeding techniques

Various studies have been conducted concerning the performance of different types of feeding techniques [42, 43]. Most common types are microstrip feed line, coaxial feed, proximity feed and aperture coupled feed as shown in Fig. 2.13. A summary of the comparison results is shown in Table 2.2.

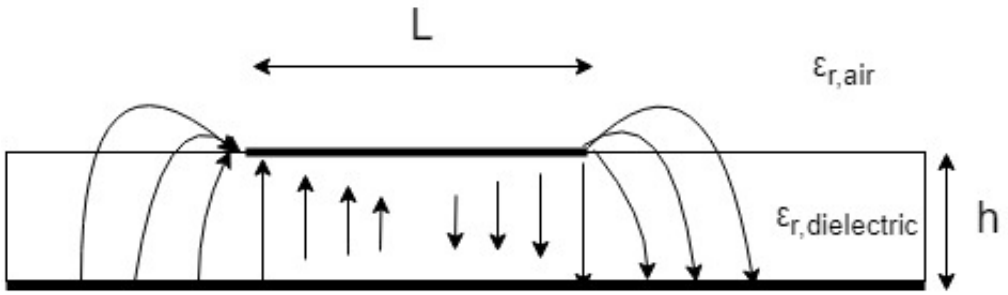

Figure 2.12: Due to the fringing effect, electric field lines propagate partly through air causing the patch antenna to radiate.

Types of feed	Spurious feed radiation	Reliability	Ease of fabrication	Bandwidth	Ease of integration
Microstrip line feed	High	High	High	2–11%	High
Coaxial feed	Low	Poor	Soldering and drilling needed	2–11%	Low
Aperture coupled feed	Medium	Medium	Alignment required	21–48%	High
Proximity coupled feed	Low	Medium	Alignment required	13–30%	High

Table 2.2: Comparison of different feeding techniques for patch antennas in terms of ease of fabrication and other metrics such as bandwidth covered, reliability of the feed and spurious radiation produced [42, 43].

Spurious radiation is caused by discontinuities or bends in the feed network, for instance when the microstrip line transforms into the patch. This radiation is limited in the other types as the feed lines are connected to the patch using connectors (coaxial feed) or use non-contact methods like aperture or proximity coupled feed. The microstrip line feed provides high reliability as it is manufactured by standard PCB processes like etching whereas the other methods require additional techniques such as soldering or precise alignment of multiple layers which can affect the functioning of the antenna making it less reliable. The aperture and proximity coupled feed provide a high bandwidth range, due to additional resonances which increases the bandwidth, as compared to microstrip line or coaxial feed which have a comparatively narrow bandwidth of 2–11%. Microstrip feed line, aperture and proximity coupled feeds provide a planar surface after fabrication but the coaxial feed requires a connector which makes the antenna non-planar. From the data presented, the microstrip line feed is chosen as the feeding method for the patch due to advantages like high reliability, easy design and planarity.

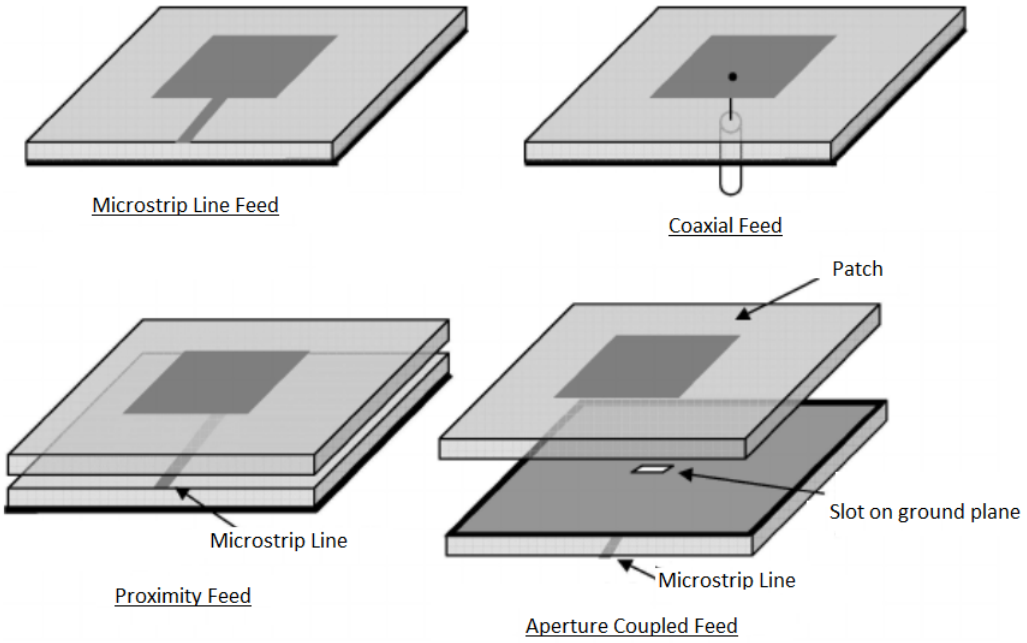

Figure 2.13: Different antenna feeding techniques used to excite the patch such as microstrip feed line, coaxial feed, proximity feed and aperture coupled feed are shown [44].

2.5.3 Overview of rectangular patch antenna parameters

For efficient radiation at a resonant frequency f_r, the width of the patch W_p is given by

$$W_\mathrm{p} \approx \left(\frac{v_0}{2f_\mathrm{r}}\right)\left(\sqrt{\frac{2}{\varepsilon_\mathrm{r}+1}}\right), \tag{2.31}$$

where v_0 is free space velocity of light.
Compared with its physical dimensions, the patch appears electrically wider due to fringing as the electric fields extend over the original dimensions. This extension is accounted for, by taking an additional section

$$\delta L \approx h\frac{(\varepsilon_\mathrm{reff}+0.3)(\frac{W_\mathrm{p}}{h}+0.264)}{(\varepsilon_\mathrm{reff}-0.258)(\frac{W_\mathrm{p}}{h}+0.8)} \tag{2.32}$$

into consideration. Using Eq (2.32), the physical patch length L can be determined by

$$L \approx \frac{1}{2f_\mathrm{r}\sqrt{\varepsilon_\mathrm{reff}\mu_0\epsilon_0}} - 2\delta L. \tag{2.33}$$

The width of the microstrip feed line W_f, used to match the characteristic impedance Z_0 to the input impedance of the patch, is given by

$$W_f \approx \frac{7.48h}{\exp(Z_0\frac{\sqrt{\varepsilon_r+1.41}}{87})} - 1.25t, \tag{2.34}$$

where Z_0 denotes characteristic impedance and t denotes copper thickness.

Width of the patch W_p and width of the microstrip feed line W_f are used for impedance matching. Better impedance matching reduces the reflection coefficient as explained in section 2.2. Feed line length does not have any effect on impedance once the microstrip line is matched to $50\,\Omega$. Increase in patch length L decreases the resonant frequency f_r. The thickness of the substrate h also influences the resonant frequency and bandwidth of the patch. Increase in thickness leads to increase in bandwidth upto a certain extent [1].

2.6 Antenna arrays

Single patch elements offer limited possibilities to modify beam pattern, gain and bandwidth. These single elements also provide wide beams in both planes. Arrays can be formed by combining multiple single elements to achieve the specified characteristics and obtain directivity in the desired direction. The radiation pattern can be controlled by various factors in the array design such as size, excitation, arrangement of the individual elements and the distance between them.

Arrays can be linear (1D) or planar (2D) in nature. Linear arrays provide a fan-shaped beam with high directionality in one plane and a wide beam in the other plane based on the array configuration. Planar arrays provide a pencil-shaped beam which is highly directional in both planes. Linear arrays satisfy the system requirements mentioned in section 3.1 and will therefore be discussed further.

2.6.1 Linear arrays

Linear uniform arrays are formed by placing N number of identical patch elements along a single line with uniform spacing d. The elements have uniform magnitude and progressive phase β between them. The array factor AF as a function of polar angle θ is given by

$$AF(\theta) = 1 + e^{j(kd\cos\theta+\beta)} + e^{2j(kd\cos\theta+\beta)} + \cdots + e^{(N-1)j(kd\cos\theta+\beta)}, \tag{2.35}$$

where k is the wave number.
Width tapering can be applied to uniform arrays to alter the beamwidth and side lobe level using array distributions such as binomial and Dolph-Tschebysheff arrays. Uniform arrays provide high side lobe level and narrow beamwidth. On the other hand, binomial arrays possess low side lobe levels with increased beamwidth. A compromise is reached between the side lobes and beamwidth using the Dolph-Tschebysheff array. Selection of the taper function is a trade-off by the designer to reduce side lobe level at the cost of increased beamwidth, details of which are discussed in section 3.4.

Array factor AF with uniform spacing and non-uniform amplitude distribution, where M elements are placed on either side of the origin and a_n is the amplitude

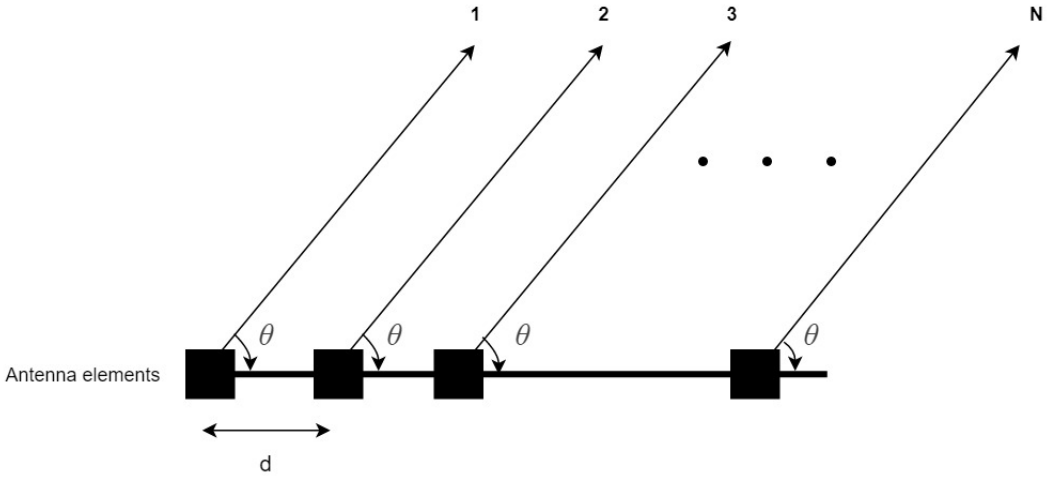

Figure 2.14: Representation of linear antenna array with N elements at a polar angle θ spaced with a distance d.

coefficient, for even and odd number of elements respectively is defined as:

$$(AF)_{2\mathrm{M}} = 2\sum_{n=1}^{M} a_{\mathrm{n}} \cos\left[\frac{(2n-1)kd\cos(\theta)}{2}\right]. \tag{2.36}$$

$$(AF)_{2\mathrm{M+1}} = 2\sum_{n=1}^{M+1} a_{\mathrm{n}} \cos\left[(n-1)kd\cos(\theta)\right]. \tag{2.37}$$

2.6.2 Antenna array feeding techniques

The feeding of the antenna array can be done through corporate-feed or series-feed as shown in Fig. 2.15. The corporate-feed network exhibits a parallel architecture consisting of multiple stages of microstrip lines and power splitters which feed each patch in the network. Each patch element in this architecture is in phase and receives equal power. However, the losses at high frequencies in this network become too high for proper operation of the array and the dimensions of the corporate-feed network become difficult to manufacture. The size of the array also doubles with each successive stage.

In series-feeding, the patches are connected serially and fed from one end. As the length of the feed lines is different for each patch, a progressive phase shift occurs between the elements which steers the main beam of the array. Though, this type of feed is more preferred at high frequencies since it is compact in size resulting in lesser loss than the corporate feed. The end-fed series-feeding technique is chosen for the current design as it is easy to design, manufacture and produces comparatively lesser loss.

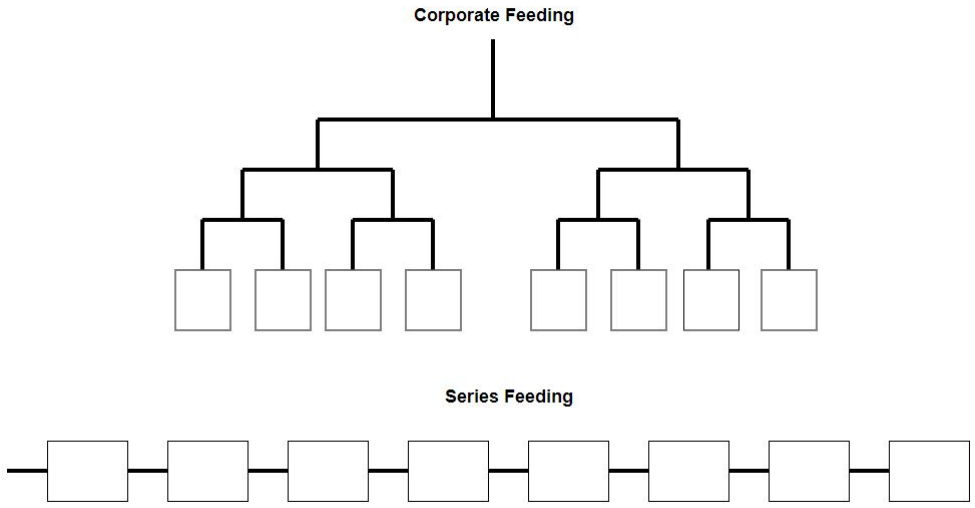

Figure 2.15: Feeding techniques for microstrip patch antenna array with parallel and series feed arrangements.

3
Methods

The mathematical formulas and design concepts discussed in Chapter 2 are used to determine the initial approximate dimensions of the antenna prototypes. These prototypes are then simulated and refined through finite element method (FEM) simulations in ANSYS HFSS which is further explained in section 3.5. The simulation workflow consisting of the modelling procedure and antenna specific settings to obtain accurate results are described. Additionally, the optimization of the antennas with respect to the most important parameters is briefly discussed.

3.1 System specifications

System specifications are derived from the requirements of the application in the tomographic system. The most important antenna parameters are beam pattern and good coupling to illuminate the object under test precisely and with sufficient signal power.

3.1.1 Frequency and bandwidth

The intended range of frequency in which the antenna operates efficiently with respect to S_{11} is 76–81 GHz. This frequency range is located in the E-band which extends from 60–90 GHz [45].

3.1.2 Half power beam width

The antenna type chosen should be able to produce a fan-shaped beam to focus the energy towards the receiver antennas in one plane and minimize reflections from the surroundings in the other plane. The HPBW specifications can be derived, according to (3.1) and (3.2), from the known system dimensions as seen in Fig. 3.1 where the TX and RX antennas are placed apart at a distance of approximately $l \approx 60$ cm and the area to be scanned is $a_1 \approx 10$ cm wide with a height of $a_2 \approx 60$cm. Therefore, HPBW is specified as $2\theta \approx 10°$ in one plane and $2\phi \approx 60°$ in the orthogonal plane to produce a beam which radiates most of the power from the antenna in a single plane.

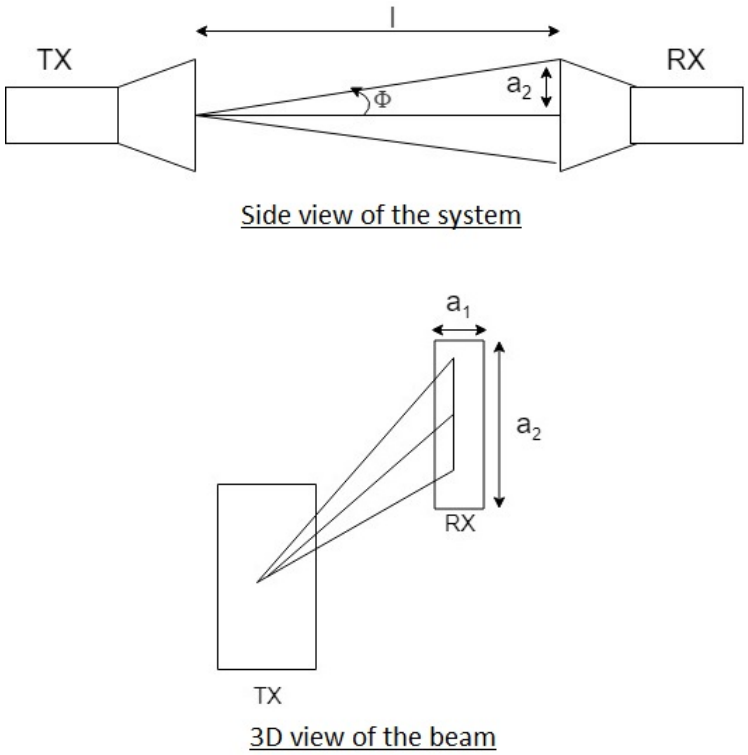

Figure 3.1: HPBW specifications are derived from known system dimensions with distance between TX and RX antennas $l \approx 60$cm and a scan area of $a_1 \approx 10$cm in width and $a_2 \approx 60$cm in height.

$$\theta = \arctan\left(\frac{a_1}{2l}\right) = \arctan\left(\frac{10}{2 \cdot 60}\right) \approx 5° \tag{3.1}$$

$$\phi = \arctan\left(\frac{a_2}{2l}\right) = \arctan\left(\frac{60}{2 \cdot 60}\right) \approx 30° \tag{3.2}$$

3.1.3 Reflection coefficient (S_{11})

S_{11} is a measure of reflected power at the input whose most widely accepted value is -10 dB. It is intended to be below -10 dB over the stated frequency range for the current work which indicates that 10% of the power is reflected back to the source.

3.1.4 Gain

The prototypes are not designed for a specific antenna gain due to a short transmission distance. The gain is determined by the beam shape and can be any positive value as long as adequate signal power reaches the receiving antenna.

3.1.5 Impedance

Industry standards for RF equipment usually define ports to have 50 Ω wave impedance. The antenna prototypes should be designed to match this value.

Horn length R_1	HPBW
5λ	37°
10λ	21°
30λ	12°
100λ	14°

Table 3.1: HPBW for different horn lengths R_1 with flare angle $\alpha = 20°$.

3.1.6 Polarization

The antenna prototypes are specified to have linear polarization as it is the most common polarization type used and this enables operation of the prototypes with other antennas.

3.1.7 Maximum dimensions of prototypes

The horn antenna prototype is fabricated using the process of 3D metal printing which will be discussed in section 3.2. The 3D printer used has maximum allowable dimensions of 89 mm × 89 mm × 100 mm which are taken as the maximum dimensional limits of the designed horn. To integrate planar antennas onto existing radar sensor PCBs, the patch antenna should occupy a maximum area of 50 mm × 50mm.

3.2 Design of H-plane sectoral horn antenna

Some parameter values can be derived directly from the system specifications. The horn antenna is designed to operate at center frequency $f_c = 78$ GHz which lies approximately midway between 76–81 GHz. As the antenna is non-resonant, the effect of change in f_c within the frequency range is negligible. The center frequency $f_c = 78$ GHz in terms of wavelength gives $\lambda = 3.84$ mm. The dimensions of the standard waveguide WR-12 are $a = 3.09$ mm in width and $b = 1.54$ mm in height [46].

As the antenna is designed to be highly directive, this will lead to high gain as the efficiency of horn antennas is typically high. Therefore, the exact value of gain is not significant. As a result, the design of the horn mainly focuses on achieving the specified beamwidth. Fig. 3.2 shows HPBW as a function of flare angle α for different horn lengths R_1. An increase in α enhances the aperture size which in turn, decreases the beamwidth as long as the phase error is constant. However, when the phase error escalates, the beamwidth widens. A longer horn with a smaller α allows for constant phase error which is required to obtain a narrow beamwidth [1]. For a given R_1, the phase error is tolerable only until the optimum α is reached. Phase error limits horn lengths as further increase in R_1 becomes ineffective in increasing HPBW as seen in Table 3.1.

The minimum R_1 required to achieve the specified HPBW (10°) is $30\lambda = 115.2$ mm. However, this length exceeds the maximum dimensions specified. Staying within

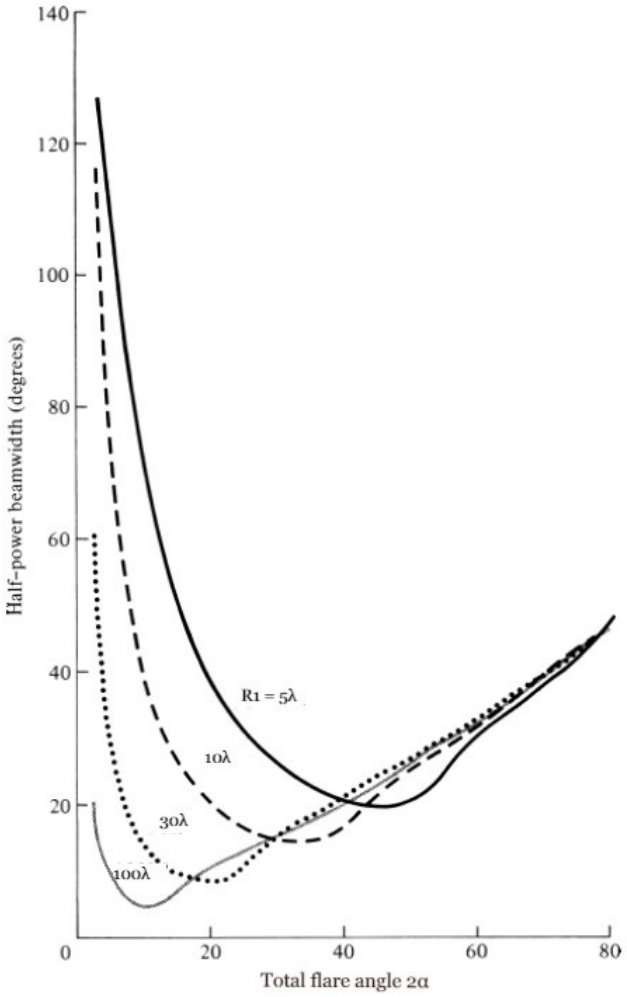

Figure 3.2: HPBW as a function of flare angle α for different horn lengths R_1 [1].

the geometrical limits of 89 mm yields $R_1 \approx 23\lambda$. To account for manufacturing tolerances, R_1 is chosen as 22λ. The corresponding total flare angle according to Fig. 3.2 is $2\alpha = 22°$ which implies $\alpha = 11°$.

After deciding on the initial dimensions, the remaining design parameters are calculated using Eq. (2.27) to (2.29) which are listed in Table 3.2.

3.3 Design of single patch element

Generally, the patch antenna covers a narrow bandwidth so it is not expected to cover the entire frequency range of 76–81 GHz. Hence, the focus of the design is to cover 76–78 GHz as the antenna will be used with a radar chip which operates with higher output power, higher linearity and less spurious signals in this range. Therefore, the mid-frequency of 76–78 GHz is chosen as the resonant frequency $f_r = 77$ GHz.

The prototype is manufactured on the substrate Rogers RO3003 with dielectric constant $\epsilon_r = 3.16$, dielectric loss tangent $\tan\theta = 0.0013$ and thickness of substrate

Parameters	Calculated Values
l_H	85.6 mm
A	26.7 mm
R_H	40.6 mm
R_1	84.5 mm
λ	3.84 mm
a	3.09 mm
b	1.54 mm
α	11°
f_c	78 GHz

Table 3.2: Values of all parameters required to design the horn antenna prototype calculated from Eq. (2.27) to (2.29) and derived from the system specifications.

$h = 0.127$ mm [47]. Rogers RO3003 is suitable for high-frequency applications owing to its low ϵ_r and low $\tan\theta$. Initial design decisions taken regarding the patch antenna are selection of rectangular shaped patch due to better gain and S_{11} [39, 48] and choice of microstrip line as the feeding method as it provides high reliability and can be easily integrated into existing systems.

The initial values of the single patch element, which are listed in Table 3.3, are determined using Eq. (2.31) to (2.34).

Parameters	Calculated Values
W_p	1.35 mm
$\epsilon_{r,eff}$	2.82
L	1.03 mm
W_f	0.255 mm

Table 3.3: Calculated values for various parameters of the single patch antenna determined using Eq. (2.31) to (2.34).

3.4 Design of patch antenna array

Single patch elements offer constrained design flexibility. Often, it is not possible to alter the beamwidth, gain and bandwidth to fulfill the system specifications. As a result, multiple elements can be combined to form an array that achieves the desired values. The number of elements in the array is decided based upon the beamwidth requirement and is a tradeoff between array size and AF. As seen in Fig. 3.3, increase in number of elements N reduces the beamwidth. This effect becomes limited with increase in N as the power available for radiation at each element decreases. Hence, the number of single patch elements in the antenna array is chosen to be 10 as no significant improvement in HPBW is seen with more elements.

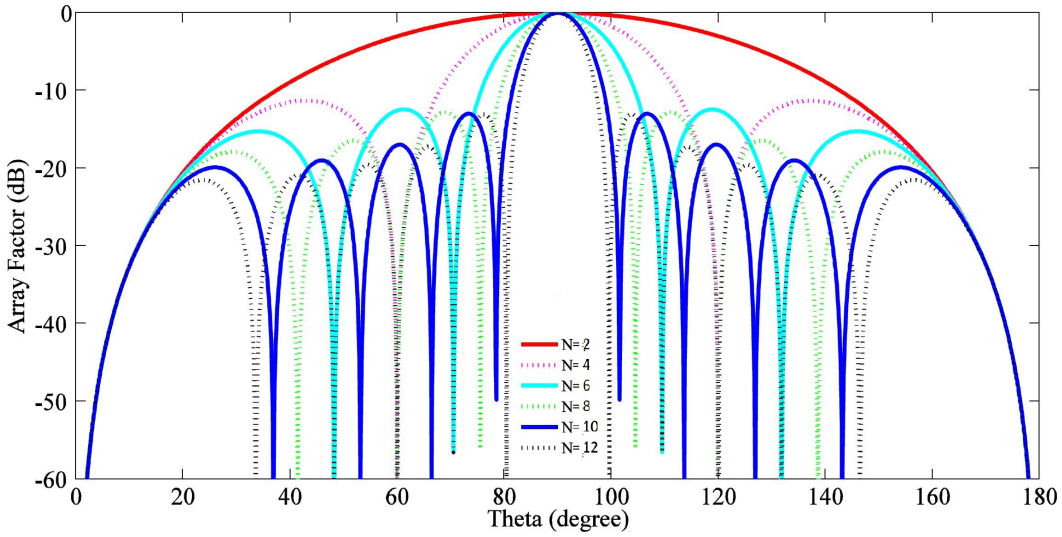

Figure 3.3: Beamwidth as a function of array factor for different number of elements N in patch antenna array. Directivity increases with increase in N but this effect is limited due to loss of power available at each element [49].

Width tapering using Dolph-Chebyshev coefficients is applied to the patch elements to reduce the side lobe levels and obtain a narrow beamwidth. The procedure of calculating these coefficients is explained in [1]. The normalized coefficients with respect to a_1, which is the amplitude of the center element, are listed in Table 3.4.

Amplitude of Element	Coefficient
$a_1 = a_2$	1
$a_3 = a_4$	0.890
$a_5 = a_6$	0.706
$a_7 = a_8$	0.485
$a_9 = a_{10}$	0.357

Table 3.4: Normalized Dolph-Chebyshev coefficients for a 10 element patch antenna array. Since the array is symmetric, the coefficients can be mirrored.

From (2.36), the array factor AF for even number of elements using the coefficients in Table 3.4 can be written as:

$$AF_{10} = \cos(u) + 0.890\cos(3u) + 0.706\cos(5u) + 0.485\cos(7u) + 0.357\cos(9u) \quad (3.3)$$

The width of each patch W_{PN} relative to the center patch W_{P1} can be calculated by:

$$W_{\mathrm{PN}} = a_{\mathrm{N}} \cdot W_{\mathrm{P1}} \quad (3.4)$$

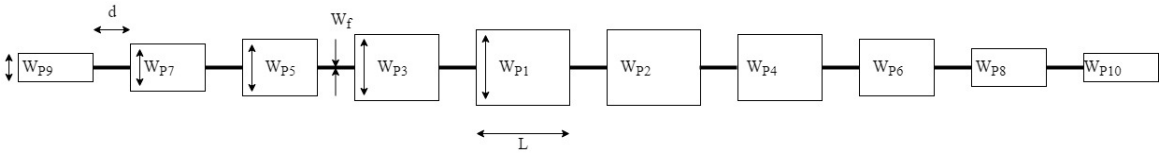

Figure 3.4: 10 element patch antenna array showcasing various design parameters such as patch length L, patch widths W_{PN}, element spacing d and feed width W_{f}.

3.5 Simulation workflow

Simulations are utilized to model and analyze real systems to reduce the time and effort required for calculations as well as measurements. They also provide a deeper insight into the behaviour of the system. The simulations are carried out in ANSYS HFSS which is a 3D electromagnetic (EM) simulator designed specifically for high-frequency applications such as antennas, RF circuits and PCBs [50]. It solves the field equations using FEM. This method divides the structure to be analyzed into small tetrahedral shaped elements collectively called the mesh. These elements are solved individually and then integrated to solve the overall structure. The mesh is refined and solved in each run of the simulation until it meets the user defined convergence criteria.

For large structures and fine mesh size, the required resources can be quite demanding. The system memory needed to execute the simulations is in the range of a few 100 GB and the computational time can vary from a few hours to a few days. The simulation workflow consists of modelling the structure, defining settings for the run, simulating the structure, analyzing the results and optimizing the model further if required.

3.5.1 Modelling of structures

Some considerations that are observed while modelling the structures in HFSS are listed below.

- The airbox, as seen in Fig. 3.5, is a region that defines the area around the model as vaccuum. The space around the structure which is not assigned a definite material is designated as perfect electric conductor. The size of the airbox should be limited as this results in fewer mesh elements leading to reduced simulation time. The radiating surface of the antenna requires a minimum distance of 0.5λ from the faces of the airbox in order for the simulator to model free space radiation correctly and prevent reflections at the boundaries.

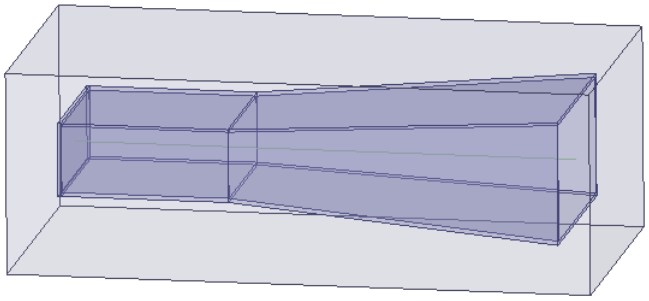

Figure 3.5: The region surrounding the structure is termed as airbox and the entire space within the airbox is simulated.

- A radiation boundary is applied to all sides of the airbox. This boundary assumes continuous propagation of the waves beyond the faces of the airbox and absorbs the energy incident normal to the surface.
- Waveport is assigned to the port as the excitation method. This method solves field distributions assuming modal vector wave propagation whereas lumped ports excite simplified field distributions for a user-defined impedance to calculate the S-parameters in terms of scalar voltage.
- The horn antenna has specified dimensions for the waveguide cross-section for modal transmission and the waveport is placed inside this area. For the patch antenna array, the height of the waveport should be between 6h to 10h and the width should be greater than $5W_f$ to ensure that the fundamental mode propagates [50].
- Symmetry boundaries provided by HFSS are utilized to model only a part of the whole structure which reduces the simulation time. Two types of symmetries that can be applied: perfect E representing a perfect electrical conductor where the E-field is perpendicular to the surface and perfect H representing a perfect magnetic conductor where the E-fields are tangential to the surface. The plane of symmetry can be applied on a surface where the symmetry is to be replicated after modelling only a part of the structure as seen in Fig. 3.6.

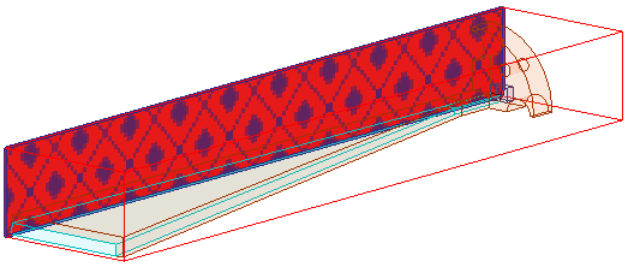

Figure 3.6: Symmetry planes E and H are applied to the surfaces of the airbox surrounding only a part of the model. Symmetry plane H is displayed in the figure. The results after simulation are replicated along the plane of symmetry.

3.5.2 Simulation settings

Assigning proper settings optimizes the resources and time required for simulations while guaranteeing accurate results. Incorrect settings will provide erroneous results even if the modelling of the structure is correct. Careful consideration of the settings is critical to avoid faulty results. The key settings are discussed below.

- The solution types relevant for antennas are driven modal, driven terminal or eigenmode. Driven modal is selected as it produces modal S-parameters in terms of incident and reflected powers whereas driven terminal produces S-parameters in terms of terminal voltages and currents. Eigenmode is used to calculate resonances of the model.
- A solution setup is added which defines the frequency at which the structure is solved along with the maximum and minimum number of passes that the mesh can be refined until the convergence criteria is met. The maximum passes sets a limit on the number of times the mesh can be refined and defines when the simulation is exited in case no convergence is reached. The minimum number of passes ensures the convergence of consecutive mesh refinements.
- The interpolating frequency sweep is adopted as it provides more accurate results compared to the fast frequency sweep and less simulation time compared to the discrete frequency sweep.
- High performance computing (HPC) enables simulation of large and complex structures on remote servers thereby reducing the computational time. HPC allows the user to define the number of parallel tasks, processor cores and memory used to solve the structure.

3.5.3 Simulation of horn antenna prototype

The design of the horn antenna in HFSS is modelled as shown in Fig. 3.7. Four of the parameters are optimized - width of the aperture A, flare length R_{H}, flare angle α and waveguide length WG as the other parameters are dependent on these. The wall thickness is specified to be 1mm to ensure a mechanically stable structure.

A waveguide flange which acts as a connector between different waveguides is added as it is present in the real system. Since the flange is made out of metal and placed very close to the antenna, it may have an influence on the radiated fields. Its dimensions are taken from the standard UG-387/U flange designed for WR-12 waveguide [46]. The material of the horn and flange is assigned to be brass.

The optimization of the design parameters is carried out without the flange using multiple parametric sweeps to obtain the narrowest beamwidth possible while keeping the other parameters such as R_1 and l_{H} within the specified size limits.

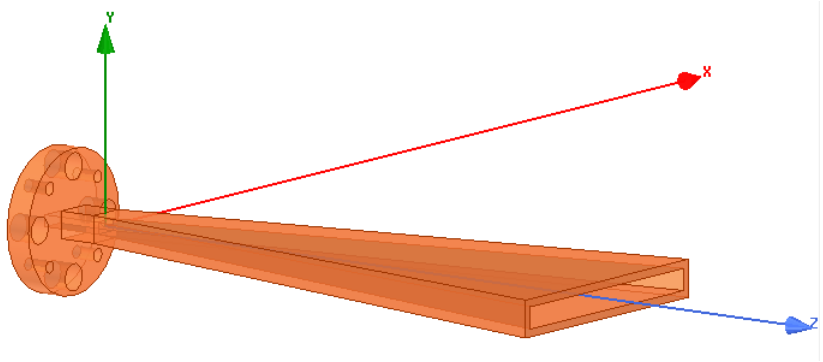

Figure 3.7: Model of horn antenna with standard WR-12 waveguide flange.

Furthermore, the design parameters are varied in presence of the flange. It is observed that varying the waveguide length WG causes an oscillation in the gain with a maxima at every half a wavelength as seen in Fig. 3.9. This phenomenon can be explained by a significant amount of backward radiation as a result of a wide beam pattern in the E-plane shown in Fig. 3.8. These backward transmitted waves are reflected off the flange interfering with the forward transmitted waves. The waves merge constructively and destructively depending on WG thereby causing the oscillation. The path difference for constructive and destructive interference is given by :

$$WG_{constructive} = \frac{N\lambda}{2}, \tag{3.5}$$

$$WG_{destructive} = \frac{(2N+1)\lambda}{4}. \tag{3.6}$$

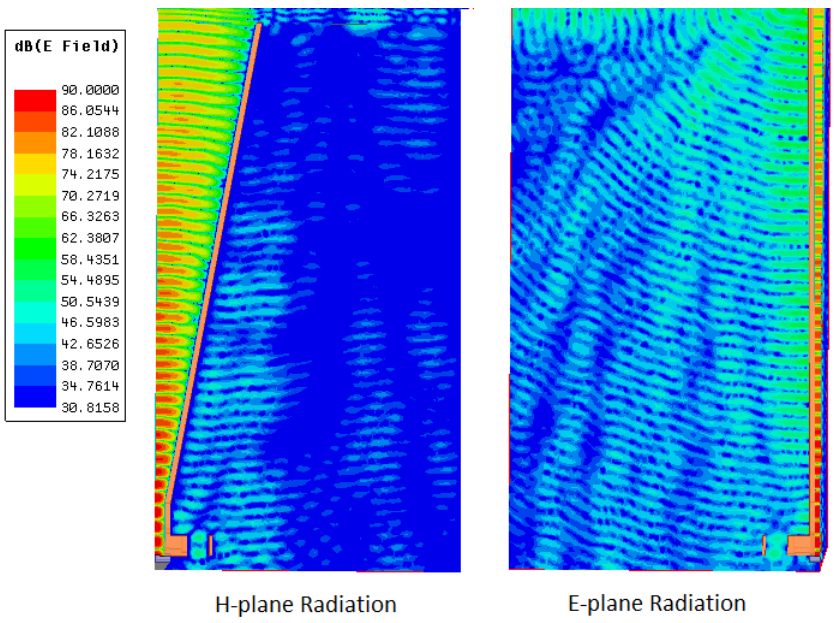

Figure 3.8: Strength of fields radiated towards the back in the H-plane are compared with the E-plane.

This implication is confirmed by simulating the structure in different scenarios (without the flange, decreasing flange radius and increasing flange radius) and varying the length of the waveguide. When the flange is removed, this results in no gain oscillation. Decreasing the radius of the flange reduces the amplitude of the oscillations whereas the opposite effect can be seen when the radius of the flange is increased which suggests that the flange acts as a metallic reflector plane behind the antenna.

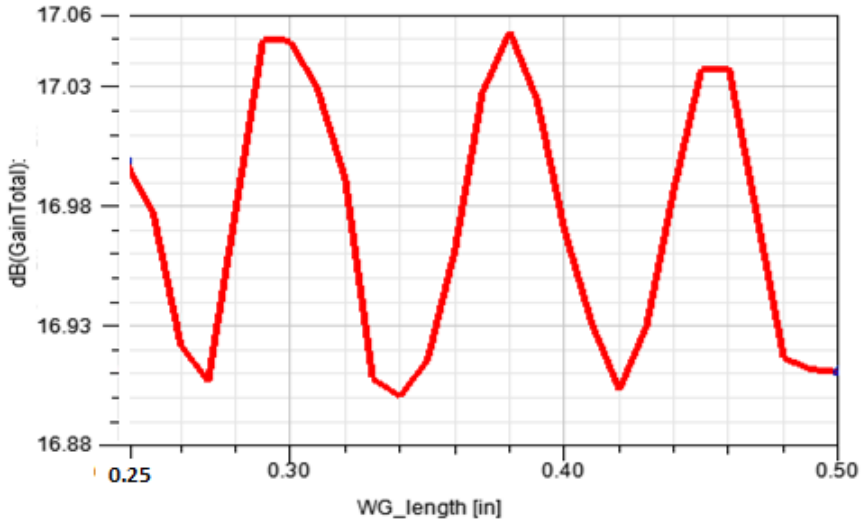

Figure 3.9: Oscillations observed in the gain at every half wavelength caused by the constructive and destructive interference of the transmitted and reflected waves.

The oscillations result in a variation of the beamwidth by 8° degrees on average in the E-plane. Due to this variation, the transmitted signal from the antenna which is setup to cover a particular range of angles in the tomographic system, may not cover the object under test completely. In simulations, the parameters can be designed such that the waves always undergo constructive interference but this is difficult to control in practice due to production tolerances. Therefore, a small flare is introduced in the E-plane to limit this variation by reducing the waves transmitted backwards.

The calculated values obtained from MATLAB and the optimized values from simulations in HFSS are compared in Table 3.5.

Parameters	Calculated Value	Optimized Value
A	32.87 mm	32.18 mm
R_H	76.58 mm	79.90
α	11°	12°
b	1.54 mm	2.87 mm

Table 3.5: Comparison of calculated and optimized values for horn antenna.

Parameters	Aspect influenced	Degree of influence
L	f_r	High
W_p	Z_0	Low
W_f	Z_0	High
d	Beam pattern	High

Table 3.6: Degree of influence of various parameters on different aspects of the design results.

3.5.4 Simulation of patch antenna array prototype

The different parts defining the structure such as patches, microstrip feed lines and substrate are modelled according to the calculated dimensions. The first design with element spacing $d{=}_1$ 0.5 λ_g between the individual patches is displayed in Fig. 3.10.

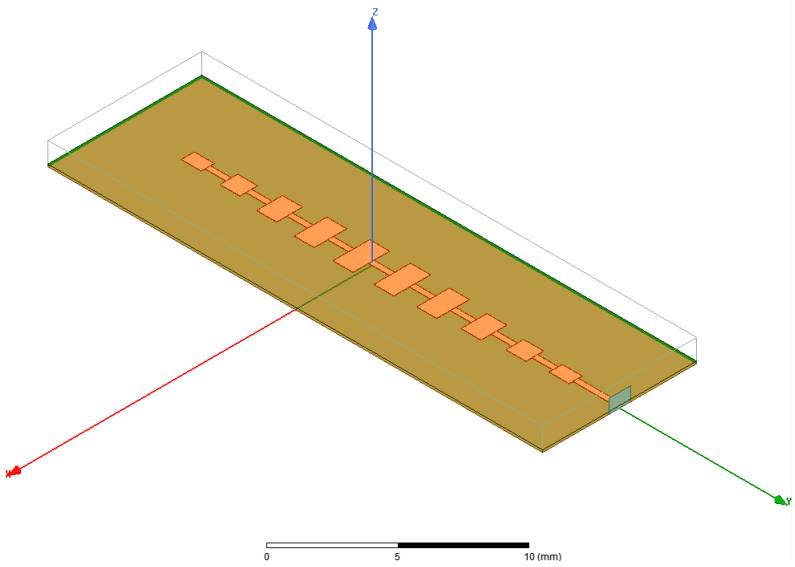

Figure 3.10: Model of patch antenna array with element spacing 0.5 λ_g.

The width of the center patches W_{P1} and consequently the width of subsequent patches along with the feed line width are varied to match the impedance as close as possible to 50 Ω.
The length of the patch L defines the resonant frequency f_r with a larger L leading to a lower f_r. L is varied in a parametric sweep to shift the resonant frequency close to 77 GHz as well as cover the lower range of the 76–81 GHz band.
The sensitivity of different parameters, listed in Table 3.6, can be derived from the influence of their variation on the design results. The calculated and optimized values are are compared in Table 3.7.

From the simulation results presented in Chapter 4, it can be concluded that the array with $d_1 = 0.5\ \lambda_g$ is not likely to fully meet the required specifications. Further increase in number of elements N has little effect on the decrease of beamwidth as explained in section 3.4. In order to further decrease the beamwidth, the element spacing d is increased. The modelling of the array with $d_2 = 1.5\ \lambda_g$ is shown in

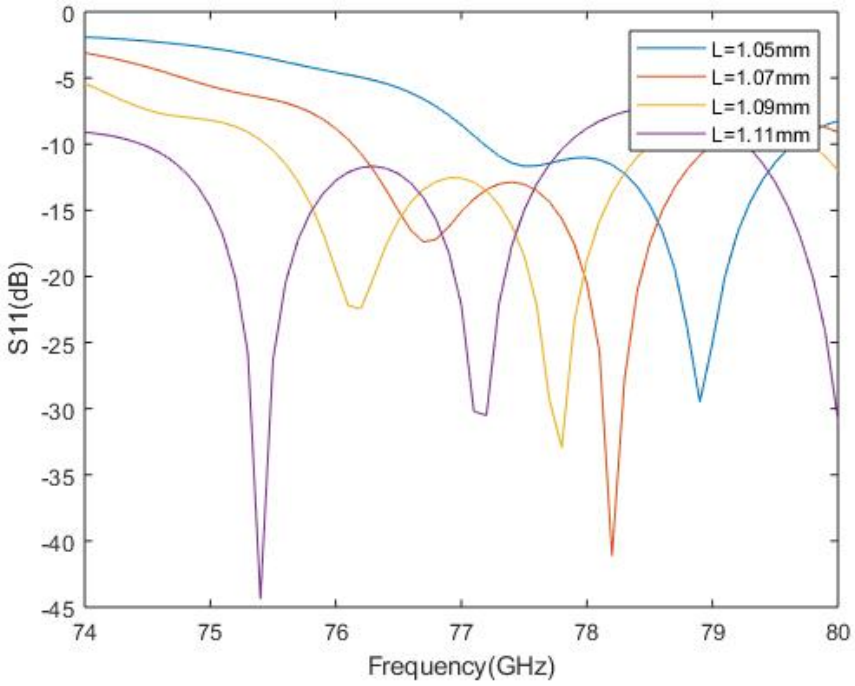

Figure 3.11: Effect of variation in patch length on resonant frequency. It is seen that f_{r} is highly sensitive to changes in L. A slight change of $L = 20$ μm causes a frequency shift of approximately 1 GHz.

Parameters	Calculated Value (mm)	Optimized Value (mm)
W_{P1}	1.35	2
L	1.03	1.09
W_f	0.255	0.3
d_1	1.16	1.09
d_2	3.48	3.5

Table 3.7: Comparison of calculated and optimized values for patch antenna array with $d_1 = 0.5\,\lambda_{\mathrm{g}}$ and $d_2 = 1.5\,\lambda_{\mathrm{g}}$.

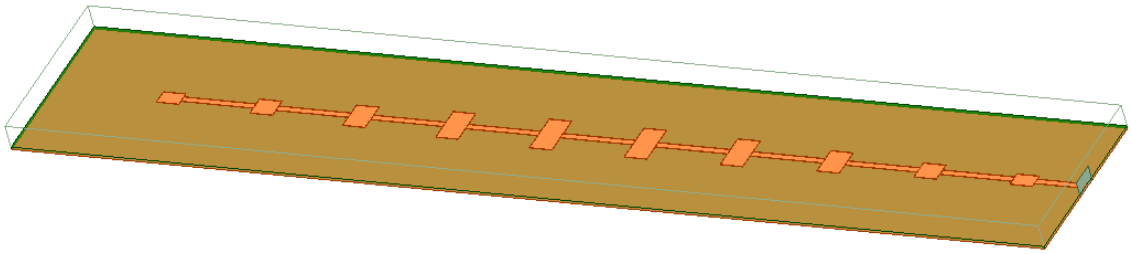

Figure 3.12: Model of patch antenna array with element spacing d=1.5 λ_g

Fig. 3.12. The dimensions of this antenna array are the identical to Table 3.7 except the element spacing is now 1.5 λ_g = 3.28 mm. The results of both the arrays are discussed in Chapter 4.

3.6 Fabrication of antenna prototypes

Prototypes of the designed horn and patch antennas are fabricated using 3D printing technology and a standard PCB manufacturing process, respectively. In the subsequent sections, each technique is explained in further detail. Additionally, the influence of production tolerances is evaluated in simulation.

3.6.1 3D printed horn antennas

3D printing is an additive process often utilized for rapid prototyping. The technology has a number of advantages compared to traditional manufacturing: factors such as short lead time, availibility of a wide range of materials and reduction in costs contribute to the increasing popularity of 3D printing [51]. However, the finished product depends on different variables like precision and accuracy of the 3D printer as well as materials used for production. The outcome may result in dimensional inaccuracy of the horn antenna leading to a change of the cut-off frequency and gain. Moreover, a higher surface roughness leads to a decrease in gain of the antenna and increase in S_{11} [52].

Two materials chosen for the horn antennas are gold plated brass and steel. Both materials are durable and have good surface conductivity required for antenna transmission. The brass prototypes have a smoother surface finish though at a higher cost. Fabrication of the brass models is done using lost wax casting. The model is first 3D printed in wax and liquid plaster is poured around it. The wax is melted once the plaster sets. Then, molten brass is poured into the plaster which is removed after the brass hardens. The finished brass antenna is electroplated with 0.25 µm of gold. The steel prototypes, composed of 60% stainless steel and 40% bronze, are produced by depositing glue on stainless steel powder forming the product layer by layer. The glue is replaced by bronze through an infusion process to create a finished structure. The guaranteed tolerances by the manufacturer are assured to be within ±5% for prototypes printed using gold plated brass whereas

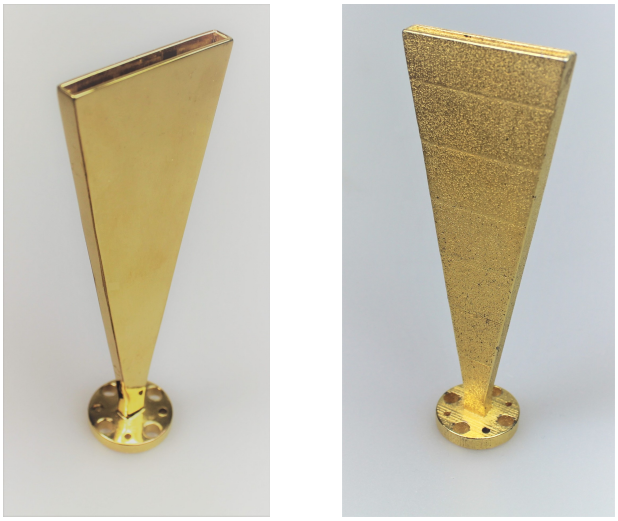

(a) Brass variant **(b)** Steel variant

Figure 3.13: Manufactured horn antenna prototypes: a) brass and b) steel variant. Steel variant exhibits higher surface roughness as compared to the brass variant which is clearly seen in the picture.

Feature (Axis)	Scaling Factor (Steel)	Scaling factor (Brass)
Length (X)	1.002	1.020
Width (Y)	0.983	1.008
Height (Z)	1.008	0.994

Table 3.8: Scaling factors of the manufactured prototypes compared to the original dimensions in length, width and height are presented.

the steel prototypes are stated to shrink by around 2.5% [53]. These tolerances are taken into account and the prototypes are scaled before production.

To consider unforeseen defects in the product, the quantity of the brass and steel variants produced was four and one, respectively. The manufactured antennas are seen in Fig. 3.13.

The originally designed prototype is re-simulated in HFSS with the measured dimensions to evaluate the effect of production tolerances. The simulations only consider scaling of the horn dimensions and do not include the effects of scaling the flange and waveguide section. The results, depicted in Fig. 3.14, show that changes in the horn antenna dimensions results in variation of S_{11}. The values of S_{11} for the scaled models are still comparable to the original S_{11} results with the maximum deviation being around 1 dB.

The manufactured models were measured using an electronic vernier caliper with an accuracy of 0.01 mm. The measured dimensions are listed in Table 3.9 and the average scaling factor in each axis for all the produced antennas is presented in Table 3.8.

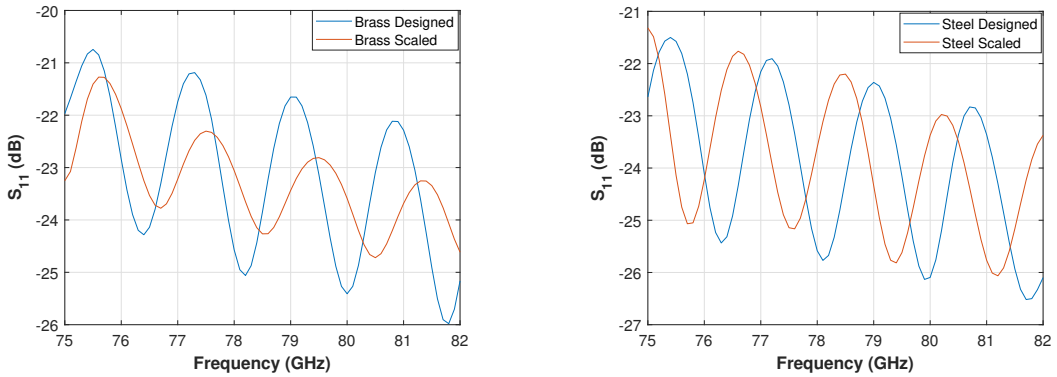

(a) Brass variant **(b)** Steel variant

Figure 3.14: Effect of scaling the original designed dimensions by the stated production tolerances for a) brass and b) steel on S_{11} for 75–82 GHz. Variation in reflection coefficient S_{11} resulting from difference between the designed and manufactured dimensions.

Parameter	Designed (mm)	Measured Steel Prototype (mm)	Measured Brass Prototype (mm)
A	32.19	31.01	32.17
B	2.87	2.65	2.87
a	3.09	2.86	2.16
Flange Radius	19.05	18.68	19.26

Table 3.9: Comparison of designed dimensions to dimensions measured for steel and brass prototypes. Width of aperture A, height of aperture B, waveguide dimension a and flange radius are analyzed.

3.6.2 Fabricated patch antennas on PCB

The designed patch antennas are fabricated on PCBs using standard production techniques [54]. The RF substrate used is Rogers 3O3003 ($\varepsilon_r = 3.16$) which is active for high frequency applications. A gold surface finish is applied to protect the copper layers underneath from being oxidized. The finish posseses a higher surface quality resulting in a smoother surface and lower losses. The tolerances are stated by the PCB manufacturer to be 10 µm of maximum expansion and 25 µm of maximum shrinkage. To minimize the influence of production tolerances, three variations of each design are produced. The original designed dimensions as well as two additional variations were fabricated on each PCB. One variation with an expanded outline and the other with a shrunk outline of 15 µm each. This results in the total length of the variations to increase and decrease by 30 µm. The manufactured PCBs are seen in Fig. 3.15 and Fig. 3.16.

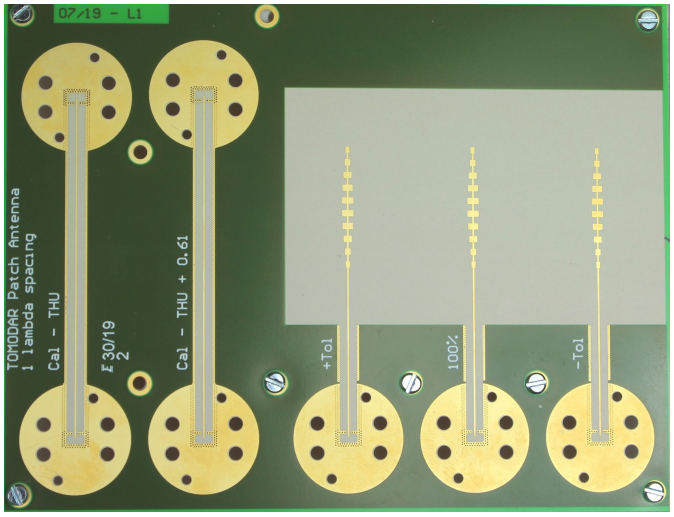

Figure 3.15: Manufactured PCB with 0.5 λ_g spacing having three variants to accommodate tolerances.

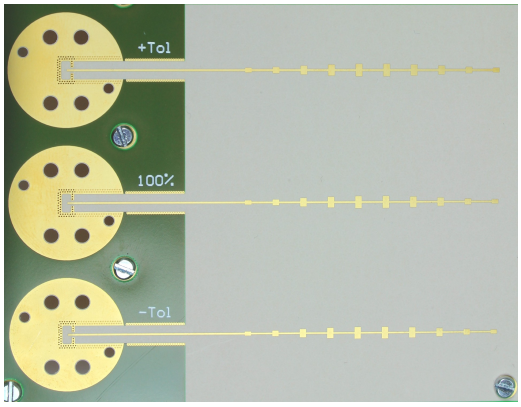

Figure 3.16: Close up of the expanded, original and shrunk variants of 1.5 λ_g spacing patch antenna array.

Simulations were performed taking these tolerances into account. The results of $d = 0.5\,\lambda_g$ and d=1.5 λ_g are shown in Fig. 3.17. It is inferred from the figures that total change in dimensions of the patch antenna array by 30 µm results in a frequency shift of approximately 0.5 GHz. This confirms that the performance of the patch antenna is sensitive to dimensional variations as discussed in section 3.5.4.

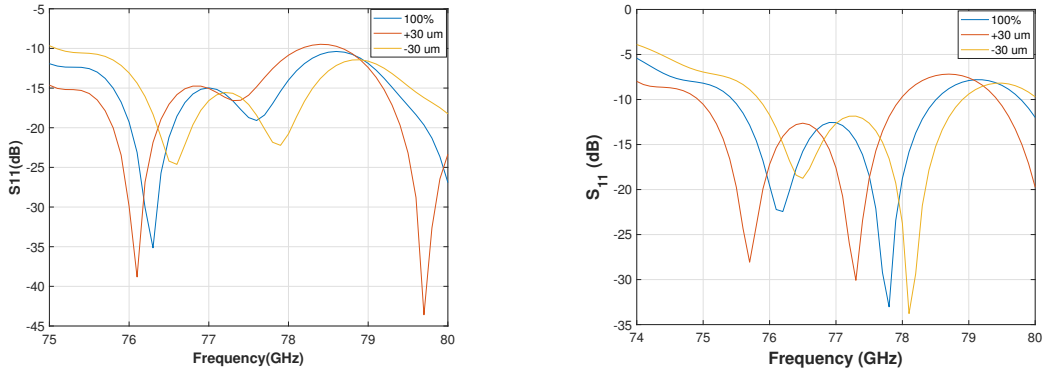

(a) 0.5 λ_g spacing **(b)** 1.5 λ_g spacing

Figure 3.17: Effect of expansion (15 μm) and shrinkage (15 μm) of patch array dimensions on S_{11} for 0.5 λ_g and 1.5 λ_g spacing.

Deembedding of the PCB is done through the Through-Reflect-Line (TRL) method, further explained in section 3.8. Calibration structures for deembedding are manufactured on the board in addition to the antenna variants. The structures have two different lengths used for the through and line measurements. A microstrip-to-WR 12 transition was utilized (insertion loss $\approx$ 1 dB) to interface the waveguide signal with the microstrip line.

The PCBs were observed under a microscope to measure the manufactured dimensions. All three variations of the patches were found to be shrunk by approximately 20 μm in length and width. This can lead to an imperfect impedance match along with a shift in the resonance frequency. A few defects such as scratches and holes in the patches and feed were also present.

Figure 3.18: Patch antenna array with 0.5 λ_g spacing as viewed under the microscope with 200x zoom.

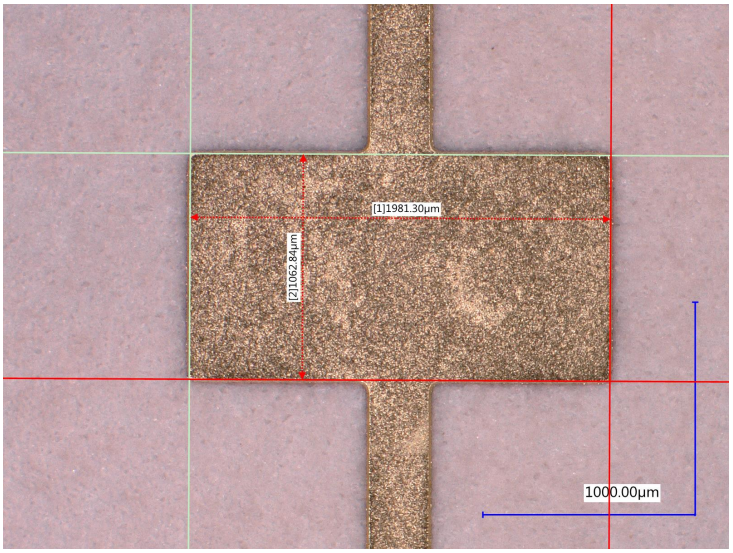

Figure 3.19: Dimensions of center patch of 1.5 λ_g spacing are shrunk by 20 μm from the original designed dimensions.

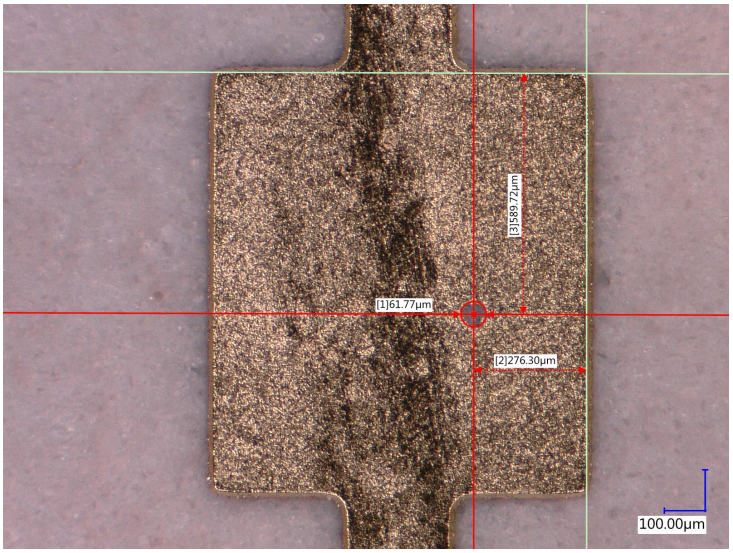

Figure 3.20: Erosion of gold surface finish and a hole of 60 μm diameter through the patch is observed.

3.7 Measurement setup

The main components required in the setup to characterize the DUT are a VNA with frequency extenders, reference antennas, and a rotary stage as displayed in Fig. 3.21. The same setup was used for the horn and patch antennas with different configurations to derive various parameters such as gain, beam pattern, reflection coefficient and cross-polarization calculated from S_{11} and S_{21} measurements.

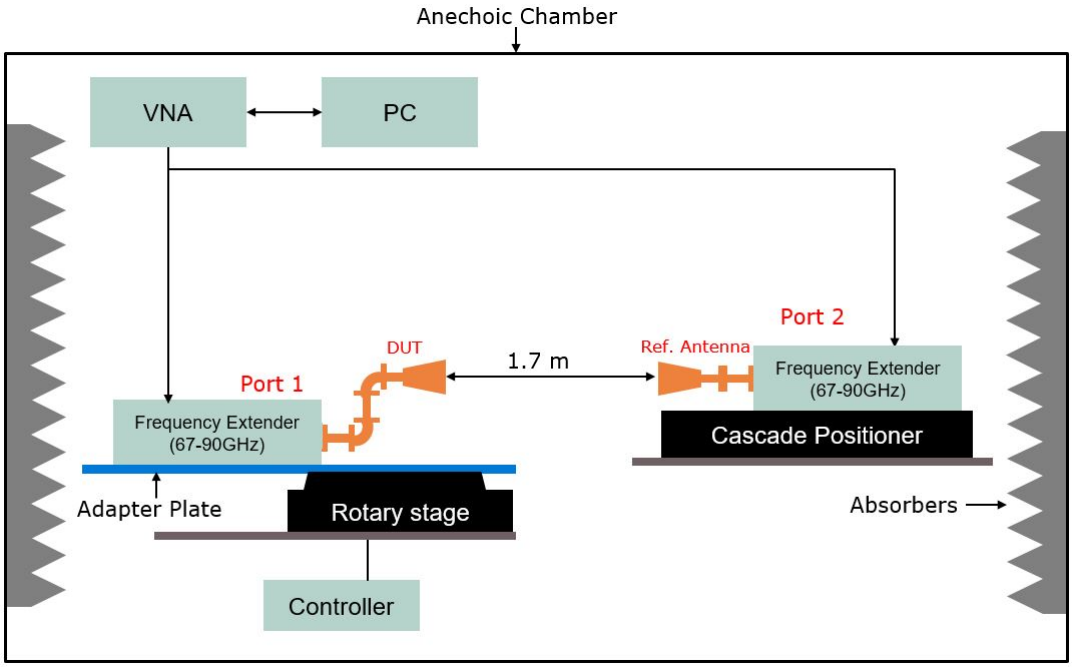

Figure 3.21: Measurement setup consisting of DUT, reference antenna, frequency extender, VNA and rotary stage in an anechoic chamber where measurements of S_{11} and S_{21} are conducted.

The VNA generates stepped frequency ramps in the frequency range 67-90 GHz that are transmitted via port 1 and received back at port 1 and port 2. This information is used to determine reflections and analyze the signal at the receiving port. The S-parameters are then calculated and displayed on the screen. The VNA settings used are given in Table 3.10.

Settings	Value
Start frequency	67 GHz
Stop frequency	90 GHz
IF bandwidth	2 kHz
Number of points	1601

Table 3.10: Values of initial settings required by the VNA to generate the measurement data. The changes in the signal are used to calculate the S-parameters.

The unknown gain of the DUT is determined using the gain comparison method which requires prior information about the gain of either the transmitting or

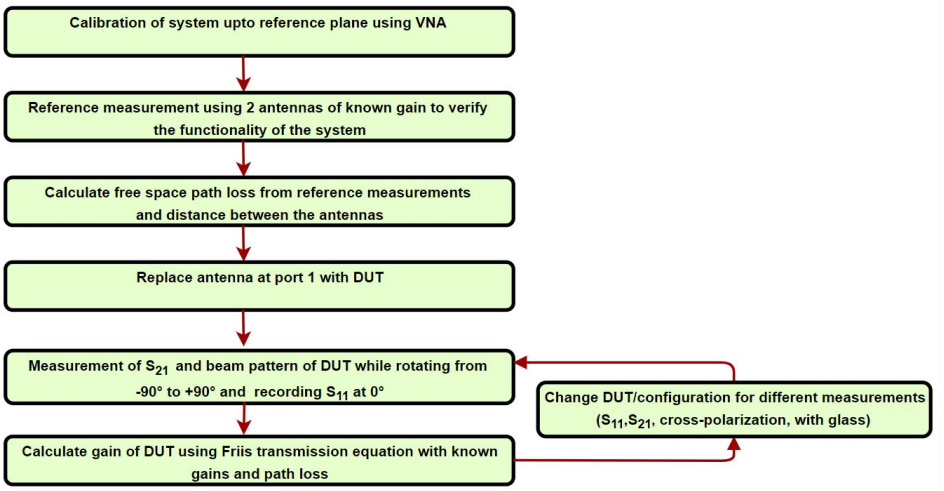

Figure 3.22: Gain comparison method includes steps such as calibration, measurements of reference antennas and measurement of DUT to calculate gain, beam pattern, reflection coefficient and cross-polarization.

receiving antenna. 20 dB standard gain horn antennas for E-band were used as reference antennas. The method to calculate the DUT gain and beam pattern is listed in Fig. 3.22 and described in the following section.

The rotary stage can be controlled manually or by software such as MATLAB. The stage can rotate clockwise or anti-clockwise depending on the software implementation. A zero position can be set and all further rotations made are relative to this position. The minimum step size of the stage used is 0.0075°.

The antenna measurements for S_{11} and S_{21} were conducted in an anechoic chamber to minimize reflections from external sources. The anechoic chamber is designed to inhibit any reflections arising due to multipath or noise from the surroundings. The interior consists of pyramidal shaped absorbers made up of carbon loaded foam which reduces unwanted signals by 40 dB in the range 67-90 GHz.

3.7.1 Measurement procedure

The system is calibrated using the two port TRL method till the reference plane of the antenna to remove the effects of other waveguide components and cables placed before the antenna. Reference measurements are executed to verify the correct functionality of the system. Initially, two standard gain WR-12 horn antennas having a gain of 20 dB are used. The distance between the antennas is 1.70 m, placing the antennas in the far field region according to (2.4). The antenna at port 1 is the transmitting antenna whereas the antenna at port 2 is the receiving antenna. The antennas are aligned in the horizontal and vertical planes using a laser distance meter and spirit level. As the gain of both antennas is

known, the path loss can be calculated using the Friis transmission equation

$$\frac{P_r}{P_t} = \frac{G_t G_r \lambda^2}{(4\pi D)^2}. \tag{3.7}$$

where P_r is the received power, P_t is the transmitted power, the ratio P_r/P_t equals the measured S_{21}, G_t is the gain of the transmitting antenna, G_r is the gain of the receiving antenna, D is the far field distance between the antennas. The path loss is represented as $(4\pi D)^2/\lambda^2$.

The theoretical value of path loss is calculated by considering the measured distance between the antennas D at frequency, 77 GHz.

$$PathLoss_{dB} = 10log\left(\frac{4\pi D}{\lambda}\right)^2 = 74.8dB \tag{3.8}$$

Value of path loss calculated from measurements is

$$PathLoss_{dB} = G_t + G_r - S_{21}(dB) \tag{3.9}$$

$$PathLoss_{dB} = 20 + 20 - (-38) = 78\ dB \tag{3.10}$$

Discrepancy in path loss obtained from calculations and measurements arises from the use of measured distance and S_{21} which may contain inaccuracies.
The antenna at port 1 is replaced with the DUT. The S_{11} and S_{21} are measured simultaneously. The DUT is rotated from -90° to +90° using the rotary stage to obtain the beam pattern in the H-plane and the S_{11} response at 0° is recorded. The step size varies from 0.75° between -15° to 15° to 1.5° between -90° to -15° and 15° to +90° to reduce measurement time of each run. The approximate location of the beam is known from the simulations and finer steps are used to record more data points in this interval.

The DUT is rotated by 90° around its axis to measure the beam pattern and S_{11} in the E-plane seen in Fig. 3.24. The same configurations are used to measure the patch antenna parameters. Cross-polarization is determined by positioning the DUT and reference antenna in orthogonal planes using a 90° waveguide twist.

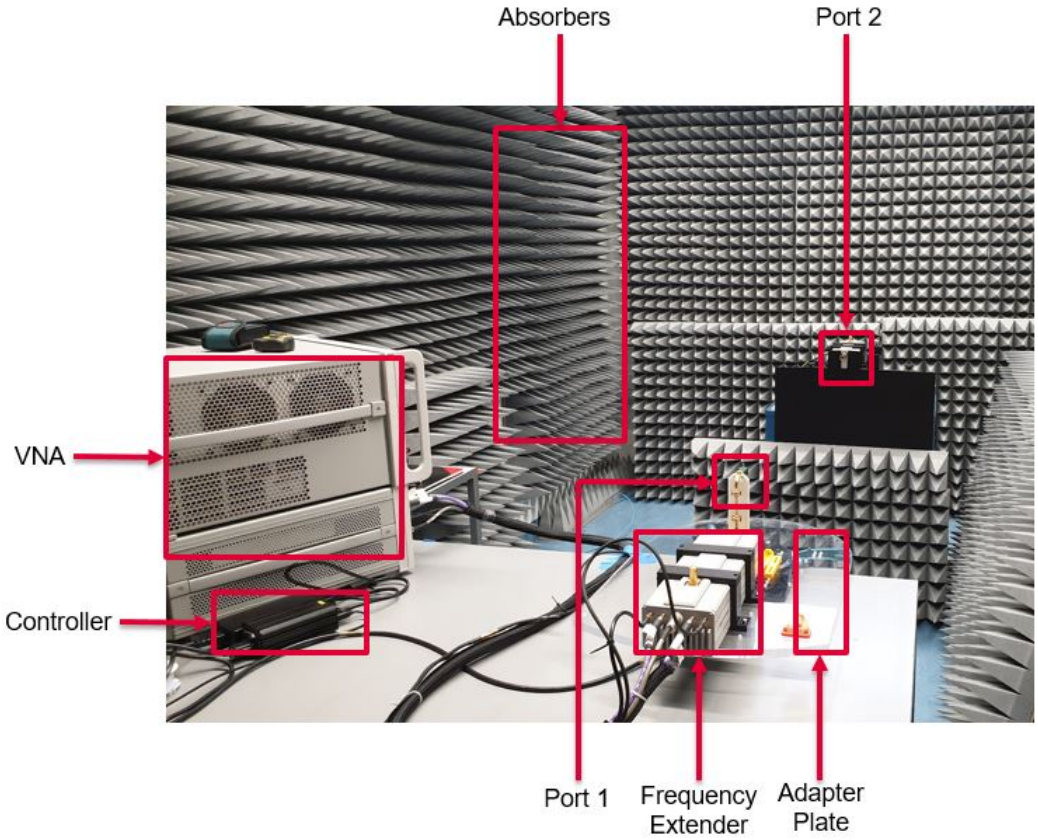

Figure 3.23: Reference measurement setup using two 20 dB standard gain horn antennas to verify the correct functioning of the system.

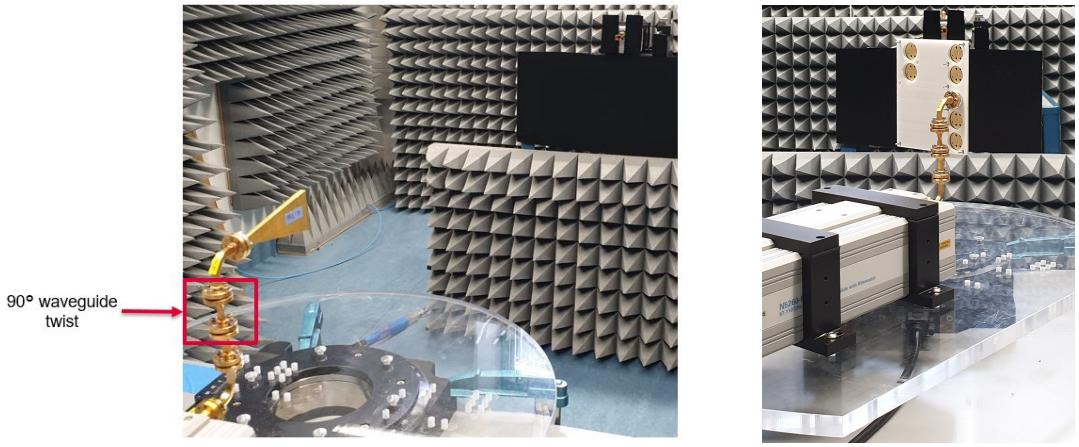

(a) Horn antenna **(b)** Patch antenna

Figure 3.24: Setup with DUT and reference antenna for E-plane measurements.

3.8 Deembedding of patch antennas

Deembedding is the process of nullifying the effects of networks other than the antenna from the measured data. Often in antenna measurements, some test fixtures may be present in addition to the antenna, for instance, a 50 Ω transmission line. The removal of the effects of these fixtures is necessary to evaluate the S-parameters of only the antenna shown in Fig. 3.25. As the test fixtures cannot be physically removed during calibration, post processing is performed in the form of deembedding to remove their influence on the results and shift the calibration plane directly in front of the DUT [55].

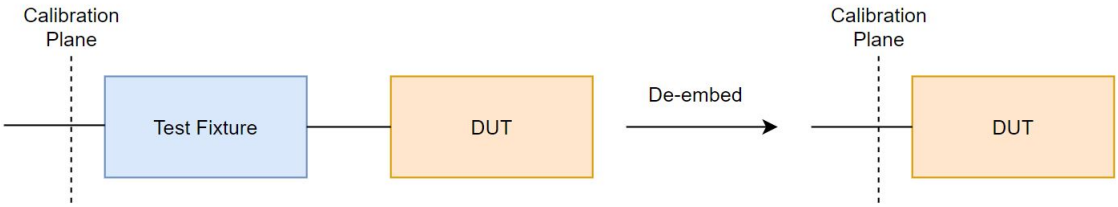

Figure 3.25: Removal of effects of the test fixture to measure the antenna S-parameters through deembedding to shift the calibration plane.

The deembedding process used is described in the following steps:

- Model the calibration structure as two cascaded symmetrical test fixtures.
- Calculate internal S-parameters of a single fixture from the calibration structure measurement.
- Create a model of the antenna system consisting of one of the symmetric fixture networks and antenna network.
- Calculate the internal S-parameters of the antenna from the measured antenna parameters and calculated fixture parameters.

The models are represented using signal flow graphs which show the direction of flow of the individual signals in the network. The cascaded networks can be represented using a single signal flow graph combining the individual network signals in order. The models are solved using Mason's rule to obtain the required S-parameters [56].

Assuming the two test fixtures making up the calibration structure are identical and symmetric: $S_{11F} = S_{22F}$, $S_{12F} = S_{21F}$. The S-parameters of the complete structure are S_{11}, S_{22}, S_{12} and S_{21} obtained through the VNA. The internal S-parameters of a single fixture are calculated as [55]

$$S_{11F} = S_{22F} = \frac{S_{11} + S_{22}}{2 + S_{12} + S_{21}}, \tag{3.11}$$

$$S_{21F} = S_{12F} = 0.5(S_{12} + S_{21})(1 - S_{11}^2). \tag{3.12}$$

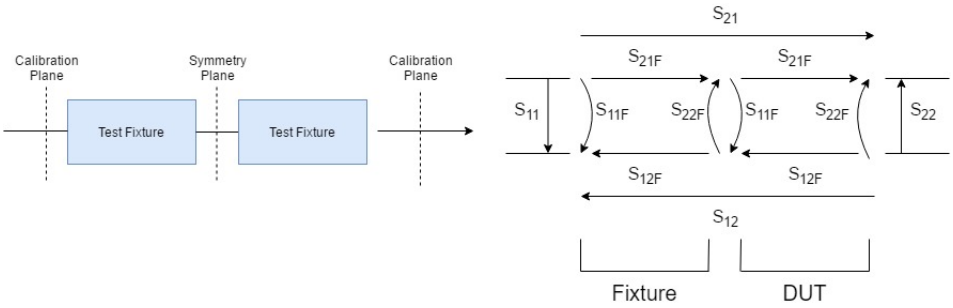

Figure 3.26: The calibration structure is assumed to consist of two symmetrical test fixtures while only one of these is placed before the antenna network. The corresponding signal flow graph describes the internal S-parameters of the two cascaded fixtures as well as the parameters obtained in calibration measurement S_{11}, S_{22}, S_{12} and S_{21}.

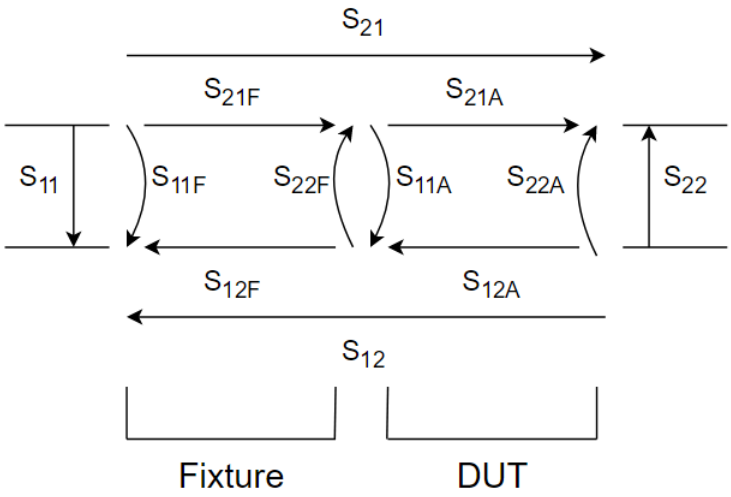

Figure 3.27: Signal flow graph showing internal S-parameters of fixture, antenna and measured S-parameters.

The model used for de-embedding is represented by the signal flow graph shown in Fig. 3.27. The model can be considered as two cascaded 2-port networks consisting of one test fixture and the antenna network. The fixture S-parameters and measured system S-parameters (S_{11}, S_{21}) are used to calculate the S-parameters of the antenna (S_{11A}, S_{21A}) using [55]

$$S_{11A} = \frac{S_{11F} - S_{11}}{S_{11F}S_{22F} - S_{12F}S_{21F} - S_{11}S_{22F}}, \tag{3.13}$$

$$S_{21A} = \frac{S_{21}(1 - S_{11F}S_{11A})}{S_{21F}}. \tag{3.14}$$

3.9 Measurement repeatibility

The repeatability of a measurement is determined by repeating the measurements under the same test conditions and evaluating the maximum deviation of the successive results. To determine the accuracy, the S_{11} measurement of the horn antenna was conducted four times in the same H-plane orientation and compared. The antenna was removed and mounted back on the VNA in between measurements. The measured S_{11} of each test is plotted in Fig. 3.28. The standard deviation of the data has a maximum value of 0.038. This indicates that the measured values are relatively close to the mean of the four data sets and the measurements have good repeatability.

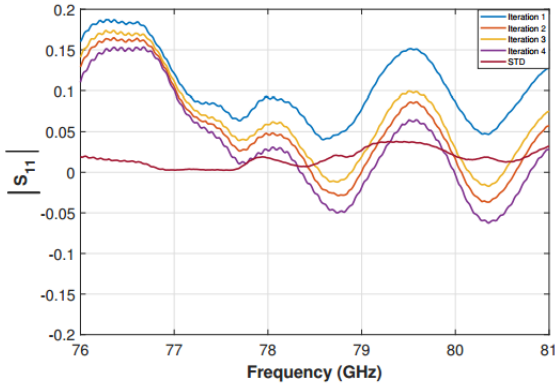

Figure 3.28: Comparison of four iterations of the same S_{11} measurement under the same test conditions is plotted. The standard deviation has a maximum value of 0.038.

4

Results

Simulated results are compared to measured results for each design and analyzed in the following sections. Simulated results are plotted in blue and measured results in orange for S_{11} and gain. E-plane and H-plane are differentiated using dashed and solid lines.

4.1 Horn antenna

S_{11} as a function of frequency is seen in Fig. 4.1. S_{11} for both variants (steel and brass) is always below –10 dB as specified and covers the entire frequency range of interest which is 76-81 GHz. Discrepancies between simulated and measured results can be explained due to misalignment of the horn antennas and waveguide components arising from a gap, offset or rotation present between them.

Fig. 4.2 shows the plot of gain with respect to angles ranging from -90° to +90°. The 3 dB beamwidth of the horn antennas can be calculated from the measured beam pattern. The beamwidth in the H-plane is 9.0° and 8.5°, in the E-plane is 64.5° and 60.0° for the steel and brass variants, respectively. The calculated beamwidths satisfy the requirements for the HPBW. These results show good alignment with simulations.

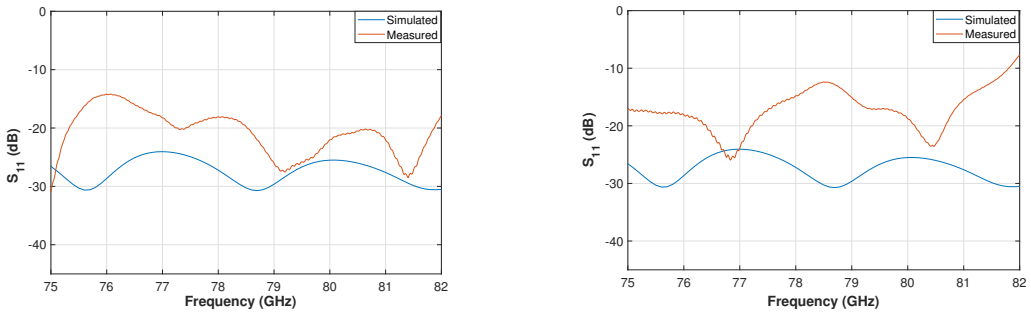

(a) S_{11} results for steel horn antenna

(b) S_{11} results for brass horn antenna

Figure 4.1: S_{11} of a) steel and b) brass horn antenna prototypes in the frequency range 75–82 GHz.

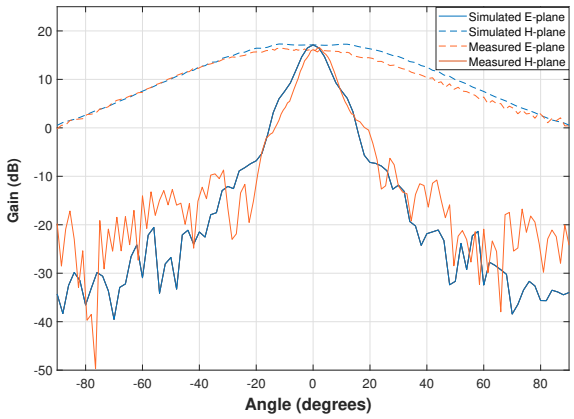

(a) Measured beam pattern for steel horn antenna

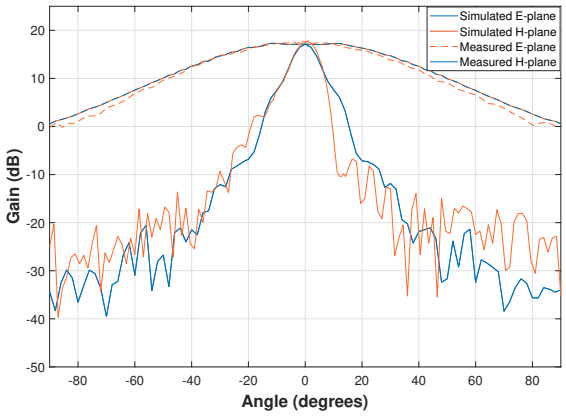

(b) Measured beam pattern for brass horn antenna

Figure 4.2: Measured beam pattern of a) steel and b) brass horn antennas in the E-plane and H-plane compared to simulated gain plot from -90° to +90°.

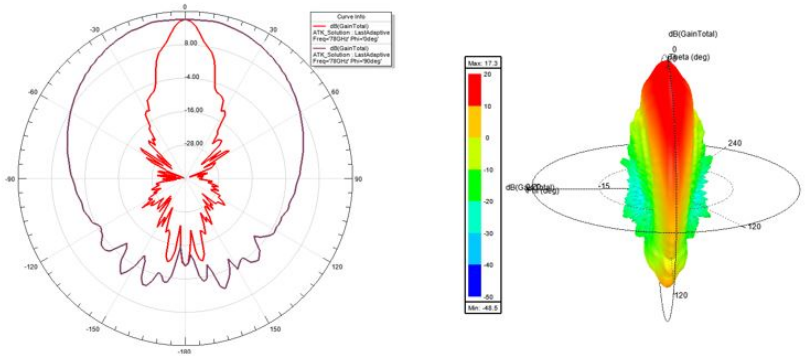

Figure 4.3: Simulated radiation pattern visualized in a) 2D and b) 3D showing the intensity and direction of the radiated beam.

The simulated radiation pattern is illustrated in 2D and 3D in Fig. 4.3. In the 2D pattern, H-plane is plotted in red and E-plane in purple. H-plane exhibits a low sidelobe level that is seen in simulation as well as measurements. The 3D pattern results in a directional beam in one plane with minimized radiation in the other plane.

4.2 Patch antenna array

Measured S_{11} results are deembedded and compared to simulated S_{11} in Fig. 4.4. For the first design with d=0.5 λ_g spacing, S_{11} is below –10 dB for the range of frequencies between 76.13 and 78.33 GHz resulting in a bandwidth of 2.2 GHz with resonance frequency at 77.15 GHz, covering most of the needed frequency range of 76-78 GHz mentioned in section 3.3. However, the specified range of 76–81 GHz is not fully covered. Improvements in S_{11} are seen in the second design with d=1.5 λ_g spacing covering frequencies between 76.49 and 80.38 GHz with bandwidth of 3.89 GHz and resonance frequency at 77.05 GHz. The enhancement in bandwidth in the second variant is due to a second resonance at 79.8 GHz. The shift in resonance frequencies between simulated and measured S_{11} is caused by the altered dimensions of the produced prototypes.

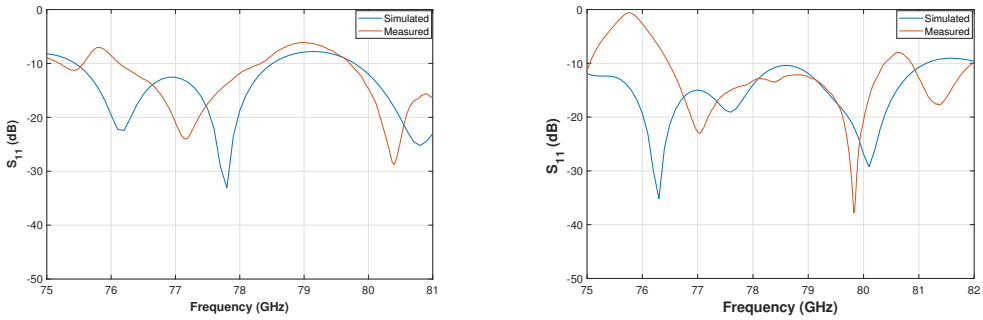

(a) S_{11} results for d=0.5 λ_g spacing **(b)** S_{11} results for d=1.5 λ_g spacing

Figure 4.4: Comparison of S_{11} results of patch antennas with a) d=0.5 λ_g and b) d=1.5 λ_g spacing in the frequency range 75–82 GHz.

The measured beam patterns of both designs and the deembedded values are plotted in Fig. 4.5. The results are listed in Table 4.1. The calculated beamwidth of d=0.5 λ_g design does not satisfy the specifications in the E-plane. Therefore, d is increased to reduce the beamwidth but a consequence of the element spacing being greater than 0.5λ is that grating lobes start to appear in addition to the main lobe. The grating lobes are located at approximately 55.0° and 65.0° and their presence does not influence the radiation of the main lobe. The antenna with 0.5λ spacing has twice the beamwidth in the E-plane compared to antenna with 1.5 λ_g spacing but it offers the advantage of no grating lobes and reduction in size.

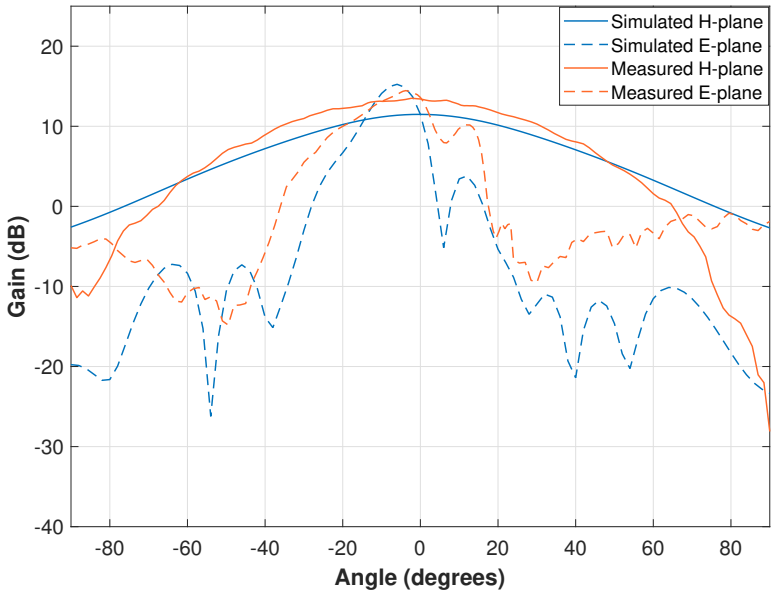

(a) Main beam with tilt of 3.5° and E-plane and H-plane beamwidth of 17.0° and 60.0°, respectively.

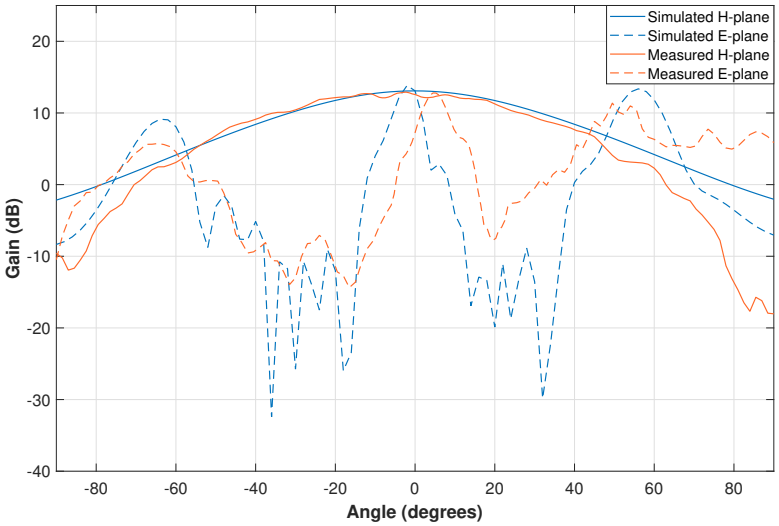

(b) Main beam with tilt of 4.5° and E-plane and H-plane beamwidth of 6.5° and 63.0°, respectively.

Figure 4.5: Measured beam patterns of a) d=0.5 λ_g and b) d=1.5 λ_g patch antennas in the E-plane and H-plane after deembedding are compared to simulated gain plots from -90° to +90°.

Simulated radiation patterns are visualized in 2D and 3D in Fig. 4.7 and Fig. 4.8. The main beams in simulation tilt by 6.0° for 0.5 λ_g spacing antenna and 2.0° for 1.5 λ_g spacing antenna. The main beam can be centered at the expense of a widened beamwidth. In measurements, the main lobe experiences a tilt of 3.5° and 4.5° for d=0.5 λ_g and d=1.5 λ_g, respectively. The tilt arises from unequal power distribution

and progressive phase shift between the elements displayed in Fig. 4.6. The results of all three designs are compared in Table 4.1.

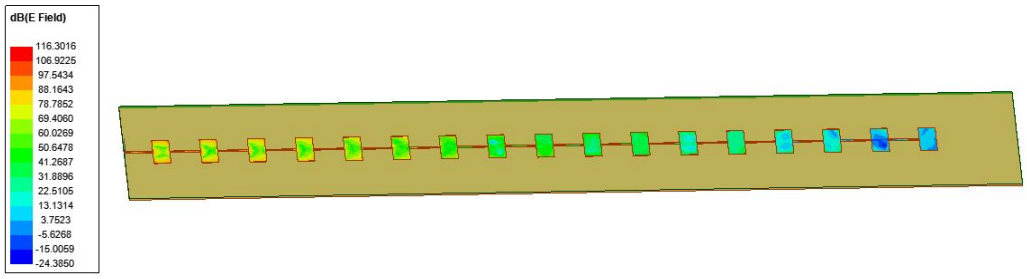

Figure 4.6: Reduction in electric field strength is seen from one element to the next. This results in unequal power distribution between the elements leading to a tilt in the main beam.

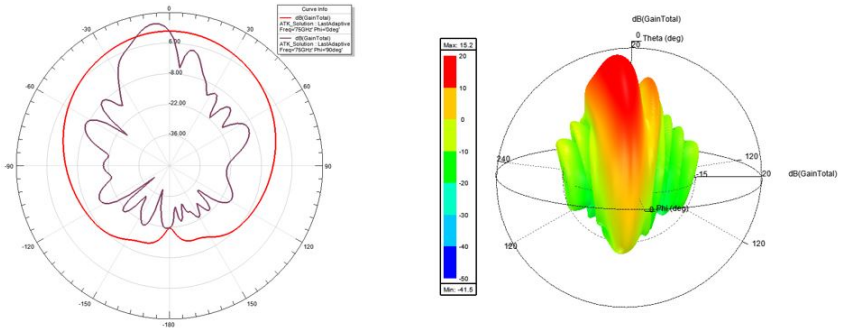

Figure 4.7: Radiation pattern displaying main beam tilt of 6.0° and beam pattern in a) 2D and b) 3D of patch antenna array with 0.5 λ_g spacing.

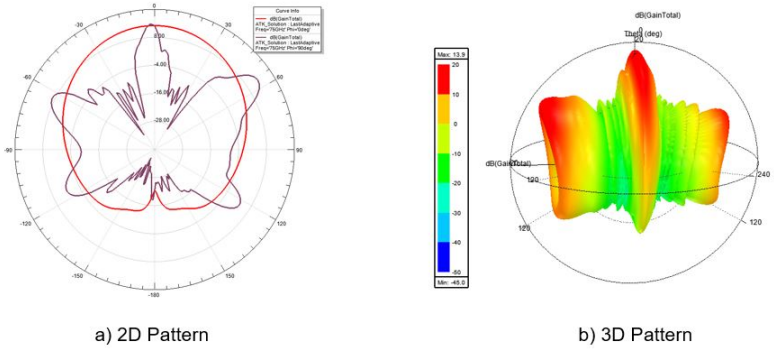

Figure 4.8: Radiation pattern displaying main beam tilt of 2.0° and beam pattern in a) 2D and b) 3D of patch antenna array with 1.5 λ_g spacing with grating lobes located at approximately ± 55.0°.

Parameter	Horn (Simulated)	Horn (Brass) (Measured)	Horn (Steel) (Measured)	Patch (0.5 λ_g) (Simulated)	Patch (0.5 λ_g) (Measured)	Patch (1.5 λ_g) (Simulated)	Patch (1.5 λ_g) (Measured)
E-plane beamwidth	63.5°	60.0°	64.5°	12.0°	17.0°	6.0°	7.0°
H-plane beamwidth	9°	8.5°	9.0°	64.0°	60.0°	62.0°	64.0°
Bandwidth	76-81 GHz (>5 GHz)	76-81 GHz (>5 GHz)	76-81 GHz (>5 GHz)	75.43-78.50 GHz (3.07 GHz)	76.13-78.33 GHz (2.2 GHz)	74.65-81.13 GHz (6.48 GHz)	76.49-80.38 GHz (3.89 GHz)
Gain	17 dB	17.5 dB	16 dB	15.2 dB	14.4 dB	13.9 dB	12.8 dB
Cross-polarization	-	-	-20.5 dB	-	-25 dB	-	-24 dB
Main beam tilt	0°	0°	0°	6.0°	4.5°	2.0°	3.5°

Table 4.1: Comparison of simulated results and results obtained from analyzing the measurements. Horn antenna and patch (d=1.5 λ_g) completely satisfy the specifications and patch (d=0.5 λ_g) partially satisfies the specifications.

4.3 System setup

The tomographic system is modelled as an octagonal quartz glass pipe with antennas as shown in Fig. 4.9. The pipe is built using eight square quartz glass slabs each of length 10 cm and thickness 2 cm. The structure has a diameter of approximately 25 cm. The dielectric constant of quartz glass is 3.78. Simulation of the entire structure is not feasible due to its large size, the simulation would need extensive memory resources and several days to complete. Hence, the setup is simplified and one scenario with a transmitting and receiving antenna is investigated in simulation and measurements. Fig. 4.10 shows the simplified setup of the tomographic system and the simulated case exploiting symmetry planes to further reduce the computational time.

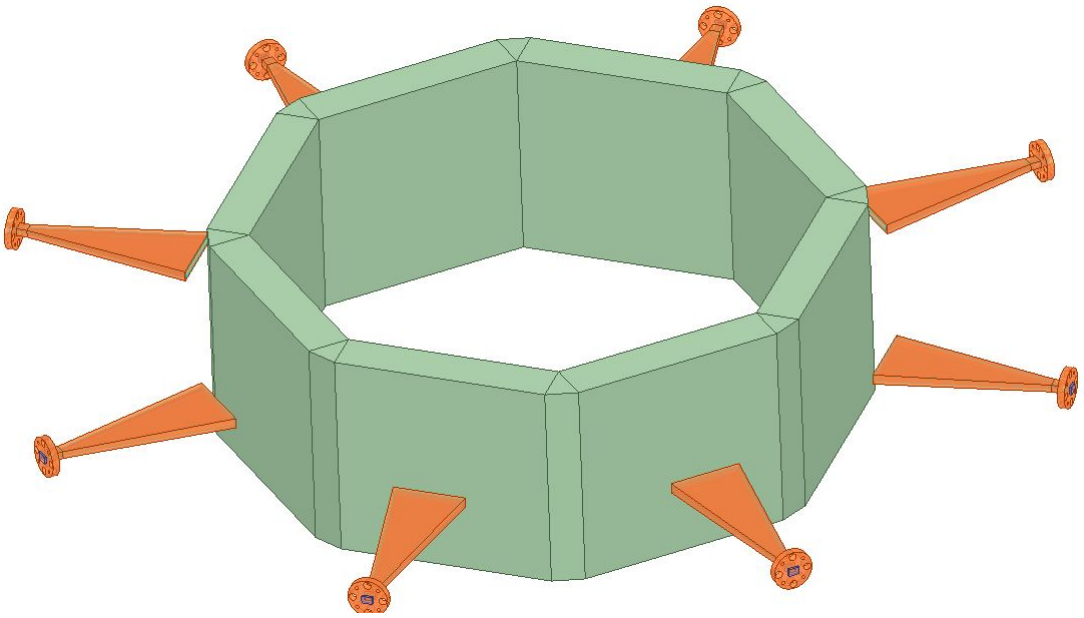

Figure 4.9: Tomographic system consisting of quartz glass pipe, transmitter and receiver antennas modelled in HFSS.

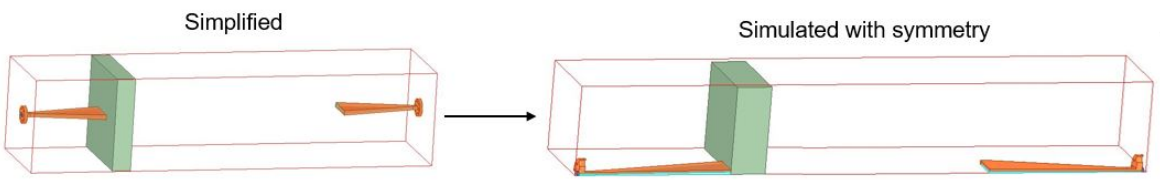

Figure 4.10: Simplified setup of the tomographic system considering one transmitting antenna, a single quartz glass slab and one receiving antenna that is investigated in simulation and measurements. This setup is simulated using symmetry planes to further reduce simulation time.

4.3.1 Return loss measurements

Measurements were carried out with a circular glass slab (diameter = 15 cm and thickness = 1.5 cm) placed at different distances from the transmitting antenna and the results are plotted and compared with simulations in Fig. 4.11.

Placing the glass close to the opening of the horn antenna results in increased reflections. As the wave travels from air in the horn antenna to glass, there is a impedance mismatch due to change in refractive index from 1 to 1.95 causing energy to be reflected back to the horn antenna. The wave does not transition smoothly as it encounters the glass surface during propagation which has a higher dielectric permittivity of 3.8 than air. Additionally, a part of the reflections is caused due to phase error present in the different travelling rays from the waveguide to the horn opening. The rays get reflected off the glass at different instants as they have slightly different physical path lengths. These reflected rays may combine constructively or destructively to give higher or lower reflections seen in Fig. 4.11. Reduced effects are observed with an increase in distance as S_{11} plot of glass at 10mm distance resembles S_{11} plot with no glass.

The demebedded results of the patch antenna with glass placed at different distances are plotted in Fig. 4.11. Similar to the horn antenna, presence of the glass increases the reflections. However, compared to the curvature of the horn antenna, the phase difference between the patch elements can be considered to be negligible and the physical path lengths are assumed to be similar. Therefore, change in the distance between the patch antenna and glass has little effect on the reflections.

The simulated and measured reflection coefficient are compared in Fig. 4.11 with glass placed at 0 mm distance from the horn antenna opening. The inconsistency between the simulated and measured results can be owed to the FEM solver used by HFSS as it does not incorporate exact optical physics to solve the models. The surface of the aperture was not perfectly parallel to the glass surface further contributing to the disparity.

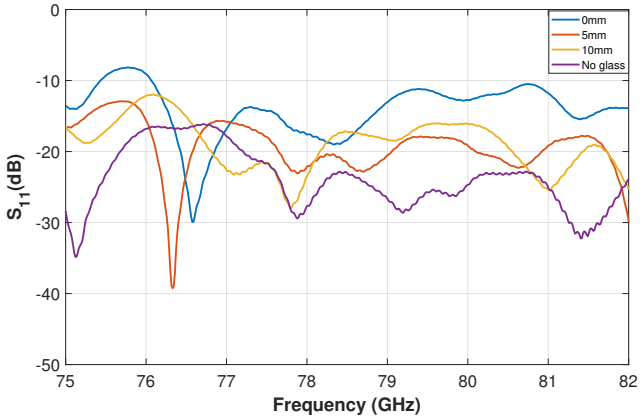

(a) S_{11} for different distances of glass from horn antenna

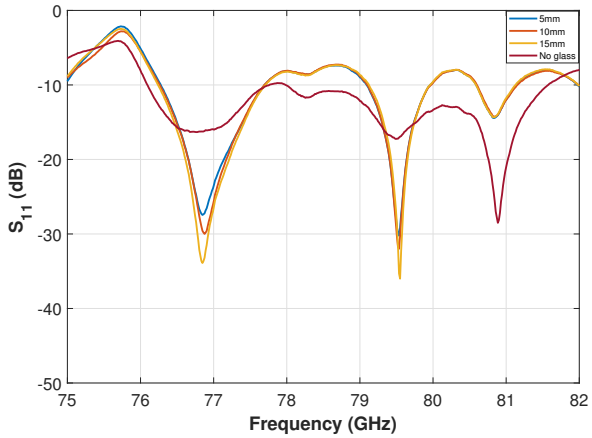

(b) S_{11} for different distances of glass from patch antenna

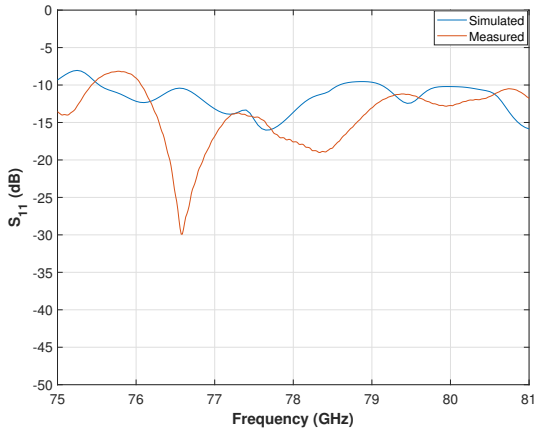

(c) Comparison of simulated and measured S_{11} of horn antenna

Figure 4.11: Effect of different distances of glass slab from antenna is seen on measured reflection coefficient S_{11} for a) horn antenna and b) patch antenna. c) Comparison of S_{11} of simulated and measured horn antenna with glass placed at 0 mm distance.

4.3.2 Refraction

Snell's law of refraction describes the relationship between angle of incidence θ_i and angle of refraction θ_r in terms of refractive indices n_1,n_2 of the media through which the wave travels. The wave bends towards the normal at the interface of the two media when it enters a medium with higher refractive index ($n_2 > n_1$). The wave bends away from the normal when it exits a medium with higher refractive index to a lower one ($n_2 < n_1$).

$$n_1 \sin\theta_i = n_2 \sin\theta_r \tag{4.1}$$

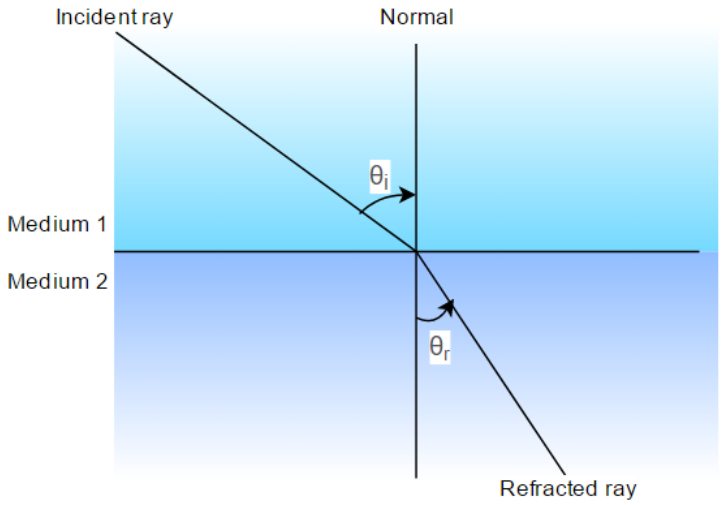

Figure 4.12: Snells's law is illustrated in the ray diagram describing the relationship between angle of incidence θ_i and angle of refraction θ_r when a ray travels from one medium to another.

The simulated electric field distribution in E-plane and H-plane of the horn antenna is depicted in Fig. 4.13. The glass has negligible effect on the H-plane of the horn, which is designed to have a narrow beam, as the angle of the rays incident on the glass is relatively small and the waves have a nearly planar wavefront. However, the E-plane beam undergoes significant refraction as θ_i is much larger and the waves possess a circular wavefront. As the beam travels from air to glass, the refraction index changes from 1 to 1.95 thereby decreasing the propagation speed of the wave in glass which is seen as shorter distance between the maxima inside the glass in Fig. 4.13. As a result, the beam bends towards the normal at the boundary. The opposite effect is seen when the beam exits the glass on the opposite side, bending away from the normal.

The measured beam patterns of the horn and patch antenna are seen in Fig. 4.14 and Fig. 4.15. In the plane with a narrow beam for both the horn and patch, negligible effects are seen as θ_i is small. The radiation pattern in the E-plane of the horn antenna exhibits a gain variation of $\pm$ 1-1.5 dB due to interference of the waves leading to a change in the beamwidth by $\pm$ 2-3°. For zero distance between the

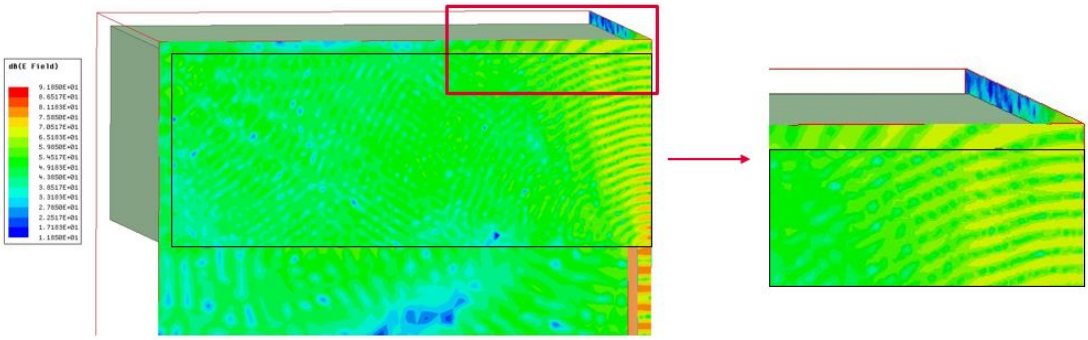

(a) E-plane beam of horn antenna exhibits refraction as the beam travels from air to glass and bends towards the normal at the interface boundary. The beam bends away from the normal while exiting the glass.

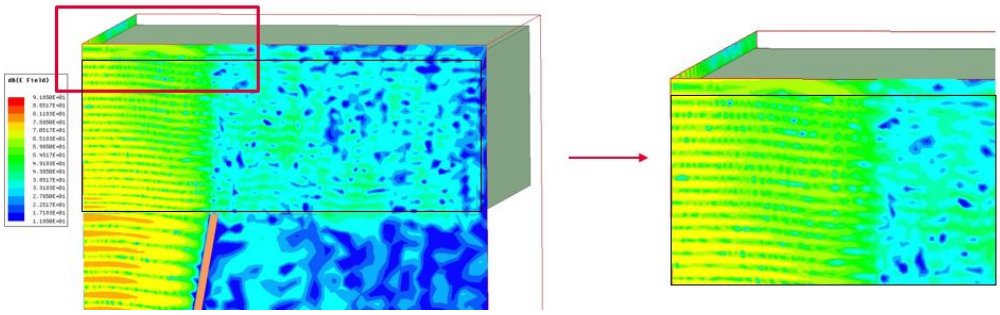

(b) Effect of refraction on H-plane of horn antenna is negligible as θ_i is small.

Figure 4.13: Simulated radiation pattern in a) E-plane and b) H-plane of horn antenna at 0 mm distance from glass. Refraction in the E-plane occurs due to larger θ_i but is limited in H-plane as θ_i is relatively small.

glass and antenna, higher fluctuation can be seen in the radiation pattern which reduces with greater distance. The lens effect of the glass affects the H-plane of the patch antenna considerably. The physical path length of the rays from each patch to the glass surface is different. Therefore, the rays are incident on the glass at different instants. Upon travelling through the glass, the waves slow down causing this difference to magnify, resulting in constructive interference causing multiple peak and destructive interference leading to reduced peak gain at different angles.

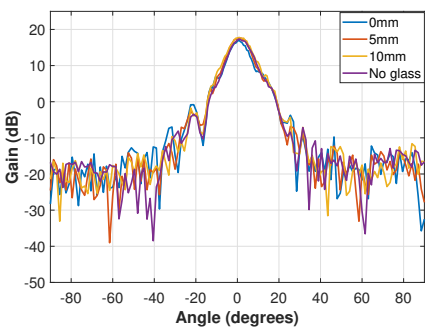

(a) Effect of refraction on H-plane radiation pattern of horn antenna

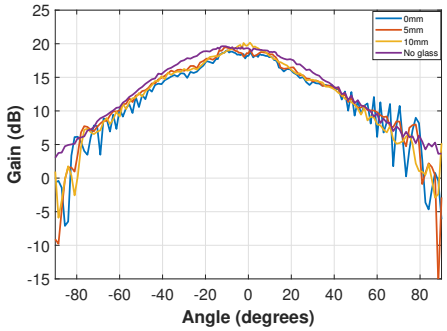

(b) Effect of refraction on E-plane radiation pattern of horn antenna

Figure 4.14: Comparison of measured radiation patterns in a) H-plane and b) E-plane for different distances (0 mm, 5 mm, 10 mm) of glass to horn antenna as well as the beam pattern with no glass present. The effect of refraction on the beam patterns due to the glass is displayed.

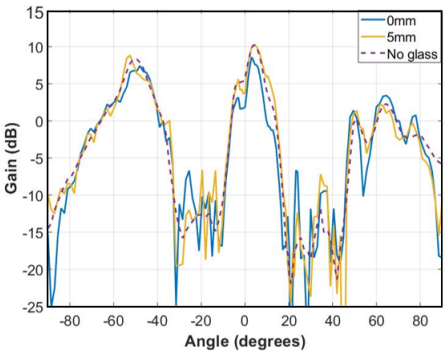

(a) Effect of refraction on E-plane radiation pattern of patch antenna

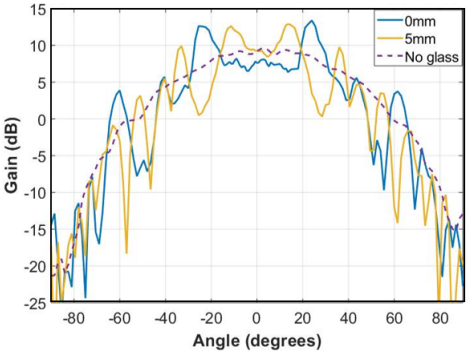

(b) Effect of refraction on H-plane radiation pattern of patch antenna

Figure 4.15: Comparison of measured radiation patterns in a) E-plane and b) H-plane for different distances (5 mm, 10 mm, 15 mm) of glass to patch antenna and the beam pattern with no glass present. The glass acts as a lens which modifies the radiation pattern due to different electrical path lengths of the individual rays in the H-plane but this effect is limited in the E-plane as θ_i is small.

5
Conclusion

5.1 Discussion

The objective of this thesis was to design, fabricate and characterize antenna prototypes in the frequency range 76–81 GHz for use in a tomographic radar system. Appropriate antenna types were selected after conducting a comparative study of different commonly used antennas at microwave frequencies. Two types, namely the horn and patch antenna array, were chosen as the focus of this thesis as they possess contrasting properties.

The first antenna prototype was chosen to be the H-plane sectoral horn antenna. Initially, the approximate horn antenna dimensions were calculated at center frequency, f_c=78 GHz. To optimize the approximate design, simulations were run in ANSYS HFSS using parametric sweeps to achieve the narrowest beamwidth. The horn antenna was produced through the process of additive 3D metal printing using two materials – steel and brass. Measurements were carried out to calculate different metrics such as gain, beam pattern and reflection coefficient to characterize the antennas. Both the manufactured antennas satisfy the system requirements with respect to the bandwidth and beamwidth in the E-plane and H-plane. Furthermore, the measured results agree well with the simulations.

The second antenna prototype developed is the patch antenna array with center frequency, f_c=77 GHz. The dimensions of the antenna were calculated using approximate equations, optimized in ANSYS HFSS and the effect of variations in the parameters due to production tolerances on the antenna properties were identified. Two variants of the antenna with different spacing between the elements were designed and produced using PCB fabrication. The first variant with d=0.5 λ_g only partially satisfied the system requirements as the narrow beamwidth is greater than the specified beamwidth of 10.0°. However, the size of the antenna array is half of the second variant with a spacing of d=1.5 λ_g and it has the advantage of no grating lobes that are present in the second variant. The d=0.5 λ_g prototype can be utilized in applications where the size of the antenna is critical. The results of the d=1.5 λ_g antenna are similar to the simulated results.

A simplified model of the tomographic radar system, for which the antennas were designed, was simulated in HFSS. One transmitting and one receiving antenna along with one glass slab were considered for simplicity in the simulations as well as measurements. Reflection and refraction based on Snell's law were observed in the results. Negligible effects were observed in the narrow plane of both the designed

prototypes. Change in beamwidth of ± 2-3° due to gain variation was seen in the wide plane of the horn antenna. The patch antenna exhibits a decrease in the beamwidth due to the constructive and destructive interference reducing the gain.

5.2 Future work

Further improvements in the antennas can be carried out by considering the suggestions listed below as they were not included in this thesis.

5.2.1 Horn antenna

- Improving impedance mismatch by filling the horn with a dielectric whose permittivity is closer to the material placed in front of the antenna to allow smooth transition of the transmitted wave and therefore reduce reflections.
- Studying effects of production related material properties such as surface roughness in simulations of the antenna.

5.2.2 Patch antenna

- Reducing grating lobes in the second patch antenna array variant by methods such as non-uniform distance between the patch elements [57, 58].
- Bandwidth enhancement of the patch antenna arrays using metamaterials or slots [59, 60].
- Incorporating the effects of the glass into the design of the antennas to achieved desired characteristics.

Bibliography

[1] C. A. Balanis, *Antenna theory: analysis and design*. Wiley-Interscience, 2005.

[2] M. I. Skolnik, *Introduction to Radar Systems*. McGraw-Hill Book Company, 1981.

[3] "ERC Report 25," 2018.

[4] K. Ramasubramanian, "Moving from 24 GHz to 77 GHz radar," 2017.

[5] H. Jia, L. Kuang, W. Zhu, Z. Wang, F. Ma, Z. Wang, and B. Chi, "A 77 GHz frequency doubling two-path phased-array FMCW transceiver for automotive radar," *IEEE Journal of Solid State Circuits*, vol. 51, 2016.

[6] C. Waldschmitt and H. Meinel, "Future trends and directions in radar concerning the application for autonomous driving," *Proceedings of the 11th European Radar Conference (EuRAD)*, 2014.

[7] B. Yılmaz and C. Özdemir, "Design and prototype of a compact, ultra wide band double ridged horn antenna for behind obstacle radar applications," *Turkish Journal of Engineering (TUJE)*, vol. 11, 2017.

[8] Z. Wu, "Developing a microwave tomographic system for multiphase flow imaging: advances and challenges," *Transactions of the Institute of Measurement and Control*, 2015.

[9] M. Mallach and T. Much, "Ultra-wideband microwave tomography: A concept for multiphase flow measurement," *German Microwave Conference*, 2014.

[10] S. Kharkovsky, P. Giri, and B. Samali, "Non-contact inspection of construction materials using 3-axis multifunctional imaging system with microwave and laser sensing techniques," *IEEE Instrumentation & Measurement Magazine*, vol. 19, no. 2, pp. 6–12, apr 2016.

[11] K. Kalyanasundaram and K. Arunachalam, "Design fabrication and evaluation of miniaturized passive and conformal screen printed electric field sensor for microwave nondestructive testing," *NDT E International*, 2016.

[12] V. Zhurbenko, "Challenges in the design of microwave imaging systems for breast cancer detection," *Advances in Electrical and Computer Engineering*, vol. 11, 02 2011.

[13] P. Mojabi, M. Ostadrahimi, L. Shafai, and J. LoVetri, "Microwave tomography techniques and algorithms: A review," *International Symposium on Antenna Technology and Applied Electromagnetics*, 2012.

[14] E. Jiya, N. Anwar, S. Bala, and E. Bello, "Microwave imaging technique for detection of multiple line cracks in concrete material," *International Journal of Human and Technology Interaction*, 2018.

[15] S. Kharkovsky, J. Case, M. Ghasr, R. Zoughi, S.-W. Bae, and A. Belarbi, "Application of microwave 3D SAR imaging technique for evaluation of

corrosion in steel rebars embedded in cement-based structures," *AIP Conference Proceedings*, vol. 1430, 2012.

[16] S. Semenov, "Microwave tomography: review of the progress towards clinical applications," *Mathematical, physical, and engineering sciences*, 2009.

[17] S. Noghanian, "Microwave tomography for biomedical quantitative imaging," 2012.

[18] Y. Kuwahara, "Microwave imaging for early breast cancer detection," 2017.

[19] D. A. Cavattoni. (Accessed May 20th, 2019) 2d radiation pattern. [Online]. Available: http://www.in3eci.it/index.php?fl=5&op=mcs&id_cont=364&eng=RADIATION$%$20PATTERN&idm=408&moi=408

[20] (Accessed May 20th, 2019). [Online]. Available: http://www.antenna-theory.com/basics/fieldRegions.php

[21] IEEE, "Standard for Definitions of Terms for Antennas," 2014.

[22] J. E. Hill, "Gain of Directional Antennas," 2001.

[23] J. Hewes. (Accessed May 20th, 2019). [Online]. Available: https://electronicsclub.info/impedance.htm

[24] M. Yavuz, "Linear, circular and elliptical polarization animation in a single shot," 2011.

[25] R. Singh and K. Mamta, "Network Analysis Of Antenna Based On Scattering Parameters," *International Journal of Industrial Electronics and Electrical Engineering*, vol. 3, 2015.

[26] D. M. Pozar, *Microwave Engineering*. John Wiley Sons, 2005.

[27] B. Mohamadzade, R. M. Hashmi, R. Simorangkir, R. Gharaei, S. U. Rehman, and Q. H. Abbasi, "Recent advances in fabrication methods for flexible antennas in wearable devices: State of the art," 2019.

[28] W. O. Alami, E. Sabir, and L. Brahim, "A H-slotted patch antenna array for 79 GHz automotive radar sensors," in *2018 6th International Conference on Wireless Networks and Mobile Communications (WINCOM)*. IEEE, 2018.

[29] E. Arnieri, A. M. Salomon, G. Amendola, L. Boccia, M. Paparo, and S. Scaccianoce, "A preliminary study on a reduced size planar grid array for automotive radars," 2015.

[30] C.-A. Yu, E. S. Li, H. Jin, Y. Cao, G.-R. Su, W. Che, and K.-S. Chin, "24 GHz horizontally polarized automotive antenna arrays with wide fan beam and high gain," *IEEE Transactions on Antennas and Propagation*, vol. 67, no. 2, pp. 892–904, 2019.

[31] H. Khazaal, H. Alrikabi, A. M. Ali, and A. K. Neamah, "Fabrication and Testing of Pyramidal X-Band Standard Horn Antenna," *Journal of University of Babylon, Engineering Sciences*, vol. 26, 2018.

[32] M. S. Meena and V. Prakash, "Simulation results of rectangular horn antenna," *International Journal of Advanced Trends in Engineering and Technology*, 2018.

[33] R. S. Piske, D. P. Rathod, and Y. S. Gothe, "Design and analysis of H plane horn antenna at X band frequency," *IJSRD - International Journal for Scientific Research & Development*, vol. 3, 2015.

[34] Z. N. Chen, X. Qing, M. S. K. Gong, and W. Hong, "60-GHz antennas on PCB," *The 8th European Conference on Antennas and Propagation (EuCAP 2014)*, 2014.

[35] M. Samsuzzaman, M. T. Islam, J. S. Mandeep, and N. Misran, "Printed wide-slot antenna design with bandwidth and gain enhancement on low-cost substrate," *The Scientific World Journal*, vol. 3, 2014.

[36] G. Eleftheriades and M. Simcoe, "Gain and efficiency of linear slot arrays on thick substrates for millimeter-wave wireless applications," *IEEE Antennas and Propagation Society International Symposium*, 1999.

[37] (Accessed May 24th,2019). [Online]. Available: http://www.antenna-theory.com/antennas/reflectors/dish.php

[38] T. A. Milligan, *Modern Antenna Design*. John Wiley Sons, 2005.

[39] M. M. Khan, A. M. Alam, and R. H. Ashique, "A comparative study of rectangular and circular microstrip fed patch antenna at 2.45 GHz," *International Journal of Scientific Engineering Research*, vol. 5, 2014.

[40] A. A. Roy, J. M. Môm, and D. Kureve, "Effect of dielectric constant on the design of rectangular microstrip antenna," 2013.

[41] K. V. Puglia, "Microwaves and RF," 2018.

[42] N. Kaur, N. Sharma, and N. Singh, "A study of different feeding mechanisms in microstrip patch antenna," *International Journal of Microwaves Applications*, vol. 6, 2017.

[43] I. Hamieh, "A 77 GHz reconfigurable micromachined microstrip antenna array," 2012.

[44] Accessed July 16th, 2019. [Online]. Available: https://www.worldscientific.com/doi/abs/10.1142/9789813208605_0001

[45] F. C. C. (FCC), "Table of frequency allocations," 2017.

[46] M. Microwave, "Datasheet 5E-031."

[47] R. Corporation, "RO3000® laminate data sheet:RO3003™, RO3006™, RO3010™, RO3035™."

[48] "Comparison of rectangular and circular microstrip fed patch antennas at 5.76 GHz," *American Academic Scholarly Research Journal*, vol. 5, 2014.

[49] S. Ur Rahman, Q. Cao, M. Ahmed, and H. Khalil, "Analysis of linear antenna array for minimum side lobe level, half power beamwidth, and nulls control using pso," *Journal of Microwaves, Optoelectronics and Electromagnetic Applications*, vol. 16, 2017.

[50] HFSS, "User guide."

[51] Tractus3D. (Accessed September 18th, 2019) 3D printing for manufacturing. [Online]. Available: https://tractus3d.com/industries/3d-printing-for-manufacturing/

[52] B. Zhang, P. Linnér, C. Kärnfelt, P. L. Tam, and U. Södervall, "Attempt of the metallic 3d printing technology for millimeter-wave antenna implementations," *Asia Pacific Microwave Conference*, 2015.

[53] Shapeways. (Accessed June 11th, 2019) 3D materials guide. [Online]. Available: https://www.shapeways.com/materials

[54] C. F. Coombs, *Printed Circuits Handbook*. McGraw-Hill Companies, 2008.

[55] Keysight, "De-embedding and embedding s-parameter networks using a vector network analyzer - application note," 2017.

[56] S. J. Mason, "Feedback theory - further properties of signal flow graphs," 1956.

[57] S. Suarez, G. Leon, M. Arrebola, L. F. Herran, and F. Las-Heras, "Linear aperiodic array of microstrip patch antennas with grating lobes reduction," 2012.
[58] B. Q. You, L. R. Cai, J. H. Zhou, and H. T. Chou, "Hybrid approach for the synthesis of unequally spaced array antennas with sidelobes reduction," 2015.
[59] C. Arora, S. S.Pattnaik, and R.N.Baral, "Performance enhancement of patch antenna array for 5.8 ghz wi-max applications using metamaterial inspired technique," 2017.
[60] S. K. Kan, L. K. Man, and C. C. Hou, "A high-gain circularly polarized u-slot patch antenna array," 2018.